

REPORT DOCUMENTATION PAGE			Form Approved OMB No. 0704-0188	
<small>Public reporting burden for this collection of information is estimated to average 1 hour per response, including the time for reviewing instructions, searching existing data sources, gathering and maintaining the data needed, and completing and reviewing the collection of information. Send comments regarding this burden estimate or any other aspect of this collection of information, including suggestions for reducing this burden, to Washington Headquarters Services, Directorate for Information Operations and Reports, 1215 Jefferson Davis Highway, Suite 1204, Arlington, VA 22202-4302, and to the Office of Management and Budget, Paperwork Reduction Project (0704-0188), Washington, DC 20503.</small>				
1. AGENCY USE ONLY (Leave blank)	2. REPORT DATE 31 May 1996	3. REPORT TYPE AND DATES COVERED Final 01 June 93 - 31 May 96		
4. TITLE AND SUBTITLE Size And Rate Effects On The Fracture Of Sea Ice		5. FUNDING NUMBERS GN00014-93-1-0714 DOD-AASERT GN00014-93-1-0714		
6. AUTHOR(S) John P. Dempsey				
7. PERFORMING ORGANIZATION NAME(S) AND ADDRESS(ES) Clarkson University P.O. Box 5710 Potsdam, NY 13699-5710 Tel: (315)268-6517 Fax: (315)268-7985		8. PERFORMING ORGANIZATION REPORT NUMBER		
9. SPONSORING/MONITORING AGENCY NAME(S) AND ADDRESS(ES) Office Of Naval Research 800 N. Quincy Street Arlington, VA 22217-5660		10. SPONSORING/MONITORING AGENCY REPORT NUMBER		
11. SUPPLEMENTARY NOTES Approved For Public Release: Distribution Is Unlimited				
12a. DISTRIBUTION/AVAILABILITY STATEMENT		12b. DISTRIBUTION CODE		
13. ABSTRACT (Maximum 200 words) This report contains the details of the experimental study as well as the theory applied to study the rate and size effect on the fracture of sea ice. To study the fracture of ice, experiments were carried out on a semi-circular bend fracture geometry. The test program formed a lab scale study to complement the in-situ large-scale sea ice fracture tests. The ice used was shipped back in the form of cores from the arctic tests. Two directions of fracture, parallel to the c-axis (optical axis) and perpendicular to the c-axis are studied. To examine the rate effect, a Reversed Direct Stress (RDS) device was modified to suit rectangular shaped test specimens. The details of modifications are given. Ice samples were subjected to creep-recovery loading and allowed to recover. The resultant time dependent deformations were analyzed using nonlinear viscoelastic theory. Experimental results as well as the details of the nonlinear viscoelastic models are given.				
14. SUBJECT TERMS		15. NUMBER OF PAGES 80		
		16. PRICE CODE		
17. SECURITY CLASSIFICATION OF REPORT Unclassified	18. SECURITY CLASSIFICATION OF THIS PAGE Unclassified	19. SECURITY CLASSIFICATION OF ABSTRACT Unclassified	20. LIMITATION OF ABSTRACT	

FINAL REPORT

SIZE AND RATE EFFECTS ON THE FRACTURE OF SEA ICE

PROJECT TITLE: Size and Rate Effects on the Fracture of Sea Ice
PRINCIPAL INVESTIGATOR: John P. Dempsey
INSTITUTION: Clarkson University
ADDRESS: Box 5710, Potsdam, NY 13699-5710
TELEPHONE (voice): (315) 268-6517
TELEPHONE (fax): (315) 268-7985
E-MAIL: john@jpdnz.cee.clarkson.edu
GRANT/CONTRACT NO: DOD-AASERT N00014-93-1-0714
R&T PROJECT CODE: 4324842
CONTRACT START,END DATES: 7/93-05/96

19970227 013

DTIC QUALITY INSPECTED 3

ABSTRACT

This report details the work completed under DOD-AASERT N00014-93-1-0714 titled 'Size and Rate Effects on the Fracture of Sea Ice'. The first chapter contains a description of a device for uniaxial direct stress testing of ice samples. Based on the original Reversed Direct-Stress (RDS) device designed by Cole and Gould (1989), this device uses most of the original components with a few modifications. Primarily, the modified device utilizes a rectangular end cap to apply uniaxial stress to square plate-based test geometries rather than the core-based specimens of the original. Details of the new end caps, as well as a description of the bonding technique developed for attaching the specimen to them, are discussed. Also included are some preliminary uniaxial stress test results obtained from tensile strength experiments on saline ice.

The second chapter details a set of fracture experiments performed on a full depth, first year sea ice core utilizing the Semi-Circular-Bend (SCB) fracture geometry. Of primary interest was determination of the effects of a very strong horizontal c-axis alignment on the apparent fracture toughness, K_Q . Also investigated was the effect of crack orientation with respect to the basal plane on K_Q . Using closed-form solutions presented in Adamson et al (1996) for the SCB fracture geometry, values for K_Q were determined directly from load and displacement data. Finally, results of the analysis, as well as details of a full microstructural examination, are presented as a function of depth in the sheet.

In the final chapter, characterization of the nonlinear viscoelastic behavior of saline ice is discussed. Details of a creep/recovery experiment explicitly designed to evaluate the con-

stitutive properties of saline ice subjected to in-plane tensile forces are presented. Based on theory previously described in Schapery (1969) for modeling the behavior of nonlinear viscoelastic materials, a general equation for strain response due to uniaxial stress under isothermal conditions is derived. Using this equation, a very accurate preliminary constitutive model of the experimentally obtained strain data is deduced.

TABLE OF CONTENTS

ABSTRACT	2
TABLE OF CONTENTS	6
LIST OF FIGURES	9
LIST OF TABLES	10
 1 INTRODUCTION	 1
 2 A MODIFIED REVERSED DIRECT-STRESS DEVICE¹	 4
2.1 Abstract	4
2.2 Introduction	4
2.3 Background	5
2.4 End Cap Modifications	8
2.5 Endcapping Procedure	12
2.6 Experimental Results	15
2.6.1 Data Acquisition and Reduction	18
2.6.2 Monotonic Ramp Tests	20
2.7 Summary	22
2.8 Future Research	23
 3 CORE-BASED FRACTURE (PHASE VI) OF ALIGNED FIRST YEAR	

SEA ICE²	25
3.1 Abstract	25
3.2 Introduction	26
3.3 Background	27
3.4 Experimental Program	29
3.5 SCB Preparation and Setup	31
3.6 Experimental Results	35
3.7 Influence of C-Axis Alignment	42
3.8 Conclusion	45
4 A BROAD-SPECTRUM CONSTITUTIVE MODEL FOR SALINE ICE³	48
4.1 Abstract	48
4.2 Introduction	48
4.3 Creep-Recovery Experiment Details and Results	50
4.4 Uniaxial, Isothermal Constitutive Equation	59
4.5 Numerical Modeling of S2 Saline Ice Strain Response	62
4.6 Application to Monotonic Stress Ramp Data	68
4.7 Conclusion	72
5 REFERENCES	75
6 PUBLICATIONS	80
6.1 JOURNAL PUBLICATIONS	80

6.2 CONFERENCE PUBLICATIONS 80

LIST OF FIGURES

2.1	Cross-Sectional comparison of the modified reversed direct-stress device and the original RDS device designed by Cole.	6
2.2	The aluminum end cap system. From the top are the multi-bolt adapter, bearing race, spherical bearing segment and the trapezoidal shaped end cap.	9
2.3	The stainless steel end cap system. From the top are the large single bolt, the new adapter, the bearing race, spherical bearing segment and the stainless steel end cap. On the left is the assembled end cap system.	11
2.4	A fully assembled stainless steel end cap. The phenolic is attached with both epoxy and bolts due to the strength of the bond which the phenolic's machined surface can create.	12
2.5	The mounting jig used for aligning a specimen with the end caps during the endcapping procedure.	13
2.6	A specimen which has been lowered into the water filled reservoir. The second end cap, with its reservoir already prepared, is next to the jig.	15
2.7	(a) The Single Edge Notch (SENCs) and (b) Double Edge Notch Clamped Strip (DENCs) geometries.	16
2.8	(a) The polynomial curve fit of a displacement vs. time plot obtained from an LVDT during experiment T201. (b) Stress vs. Strain curves for monotonic loading from 0 – 2000 Newtons at loading rates between 1 to 1000 N/sec.	20
3.1	The processing history of Core #1 from harvest to disc form.	29

3.2	The SCB's were loaded in 3 point bending (a) with a load-controlled, linear ramp (c) until fracture occurred.	31
3.3	Load vs time (a & c) and load vs crack-opening-displacement (b & d) plots obtained from specimens FR1AE and FR1AH.	34
3.4	K_Q , E' , δ_{CMOD} and δ_{CTOD} vs depth. \perp and \parallel indicate crack propagation perpendicular and parallel to the basal plane, respectively. Each solid line is a linear best fit to the corresponding dataset.	36
3.5	Salinity, density, brine volume and porosity vs. depth. Below are Schmidt equal area net pole projections (arrow indicates North or 180°) at various depths through the sheet.	41
4.1	(a) Location of specimen T302 in the original ice sheet, (b) Stress was applied to the ice along the length of the columns, producing a stress field similar to in-situ, in-plane tensile forces.	51
4.2	The modified Reversed Direct Stress (RDS) device.	52
4.3	Strain response was measured with cantilevered gage mounts over both the central 80%, and the full length of the specimen. Parts (a) and (c) show the gage positioning on the left and right sides (from the front view (b)), respectively.	54
4.4	Stress vs time as recorded during experiment T302. The number on each segment indicates the duration of each creep and recovery period (in minutes).	55

4.5	Strain vs time data obtained from the LVDT gages. Graphs (a) & (b) show the similarities between gages mounted on the same specimen face, (c) depicts the difference in strain between the opposing faces and (d) is the four gage average used for numerical modeling.	57
4.6	Schmidt equal area net pole projection for the saline ice used in experiment T302.	58
4.7	An idealized representation of the creep and recovery of a linear viscoelastic material. (After Schapery, 1969)	60
4.8	(a) Idealized representation of a nonlinear creep-recovery strain history. (b) Data from this creep-recovery experiment shows that from (a), $B = C$, and therefore the stress functions $g_1 = a_\sigma = 1$	64
4.9	(a) Experimental and model strain response obtained with the given model parameters and (b) the individual model strain components.	67
4.10	(a1) - (c1) Experimental and model strain response to monotonic stress ramps and (a2) - (c2) the individual strain components of each model.	70
4.11	(d1) - (f1) Experimental and model strain response to monotonic stress ramps and (d2) - (f2) the individual strain components of each model.	71

LIST OF TABLES

2.1 Uniaxial tension test results 21

3.1 SCB easy fail fracture test results 38

3.2 SCB hard fail fracture test results 39

1 INTRODUCTION

Over the past several years, the issue of size effect on the fracture and strength properties of polycrystalline ice has increasingly become the focus of laboratory and field testing. One major contributor to this ongoing study has been the Office of Naval Research through its Accelerated Sea Ice Mechanics Research Initiative (SIMI) project. The goals of their sponsored research are varied, but the overriding theme has consistently been to obtain fracture and constitutive data over the scale range from laboratory size (0.1 m) to regional size ($\approx 1,000$ km). The ice mechanics group at Clarkson has been involved in determining the fracture and constitutive behavior of sea ice in the range of 0.1 - 100 meters. This thesis is a collection of work that has been done at the small or laboratory scale, concentrating on the tensile, fracture and creep properties of sea and saline ice in conjunction with the large scale field program (Adamson et al, 1995).

In the first chapter, a loading device designed to apply constant, uniaxial tension or compression on ice specimens is described in detail. This device is based on the original Reversed Direct Stress (RDS) device developed by Cole and Gould (1989) for zero mean stress cyclic constitutive testing of core ice samples. With the modifications presented, the new device is capable of producing a constant, reversible stress field in rectangular plate ice specimens. The two primary issues which the device was designed to address are the nonparallel end planes of machined ice specimens and the lack of a uniaxial loading apparatus which remains rigid when the load transfers between the tensile and compressive regimes. Both of these problems are solved by a set of specially designed end caps which adapt the

misaligned specimen with the testing frame and that can then be hydraulically clamped in place. Also presented is the procedure for bonding the specimen to the end caps and some preliminary tensile test data.

To further develop the link between laboratory and field scale testing of sea ice, each Phase of the SIMI project included a set of laboratory scale experiments. In Phase VI however, there were no small scale tests performed due to the rigorous field testing schedule. Therefore, to remain consistent in providing both field and lab scale data in each stage of the first year sea ice growth, three full depth cores were removed from the Elson Lagoon ice sheet and shipped back to Clarkson University to complete the laboratory scale analysis. Chapter 2 describes the subsequent set of 26 Semi-Circular Bend (SCB) fracture experiments performed on specimens cut from one of the full depth cores. Due to the presence of tidal currents in Elson lagoon, the ice sheet developed a very strong c-axis alignment parallel to the tidal water flow. The effects of this strong c-axis alignment on the apparent fracture toughness K_Q and the modulus E' were the primary focus of this investigation. Upon completion of the experiments, a thorough microstructural analysis of the ice was performed. Ultimately, K_Q , E' , crack-mouth and crack-tip-opening-displacements, salinity, density, brine volume and porosity are plotted versus depth in the sheet.

In the final chapter, the RDS device detailed in the first chapter is used to apply uniaxial, isothermal creep-recovery loadings to a S2 saline ice sample. By the orientation of the sample in the device, the ice is subjected to loading similar to that of in-plane tensile forces in an in-situ sheet. Using the theory outlined in Schapery (1969, 1996), a theoretical model of

the strain response to the creep-recovery loadings is derived. Based on the strain response recorded in the experiment, each parameter of the creep-recovery model is then determined numerically to provide a best fit of all cycles in the experimental data. With the parameters defined, the model is expressed in general form for any arbitrary stress history.

2 A MODIFIED REVERSED DIRECT-STRESS DEVICE¹

2.1 Abstract

A device for uniaxial direct stress testing of ice samples is described. Based on the original Reversed Direct-Stress (RDS) device designed by Cole and Gould (1989), this device uses most of the original components with a few modifications. Primarily, the modified device utilizes a rectangular end cap to apply uniaxial stress to square plate-based test geometries rather than the core-based specimens of the original. Details of the new end caps, as well as a description of the bonding technique developed for attaching the specimen to them, are discussed. Also included are some preliminary uniaxial stress test results obtained from tensile strength experiments on saline ice.

2.2 Introduction

Direct uniaxial stress testing has generally been accepted as the most accurate method (Schwarz et al, 1981) for measuring the tensile behavior of ice. The effects of stress and strain magnitude and frequency (among others) on material strength properties can be examined without the complications and uncertainty of a non-uniform stress field. With the development of the Reversed Direct-Stress (RDS) device (Cole and Gould, 1989 & 1990a) for testing core ice specimens, constitutive behavior and cyclic stress history effects (Cole, 1990b; Cole, 1995) can now be more accurately studied by utilizing its ability to apply alternating tension and compression with zero mean stress.

¹Accepted for publication in *Cold Regions Science and Technology*, July 1996.

The versatility of this device has led the authors to develop a modified version of the original RDS device for use in fracture testing. Due to its simple mechanical design, only a change in the end cap shape is needed to apply a uniform stress field to rectangular plate specimens instead of core ice samples. This preliminary paper contains a discussion on the advantages of using the RDS device for tensile and cyclic testing of ice, details of the modifications made to the end caps and a description of the techniques developed for mounting the modified end caps on plate specimens. Also included is data obtained from some preliminary uniaxial tension experiments aimed at evaluating the modified device's tensile loading performance and determining the Young's modulus and tensile strength of lab-grown saline ice. Future research with the RDS device will include tensile fracture testing of first-year sea ice with the Single Edge Notched Clamped Strip (SENCs) geometry.

2.3 Background

The original RDS device (see Fig. 2.1b) was designed for uniaxial stress testing with the goal of determining the constitutive properties of ice cores (Cole and Gould, 1989 & 1990a). Loading systems capable of imparting states of uniaxial stress are not new; universal joints and ball seats have been used by several researchers (Currier and Schulson, 1982; Mellor et al, 1984; Sinha, 1989; Richter-Menge and Jones, 1993). The RDS device has one major advantage over these loading systems. Specifically, once a specimen has been clamped in the device it is held rigidly in position, allowing the load actuator to not only apply a constant stress field, but also to transfer smoothly between tensile and compressive regimes.

The initial development of the RDS device was driven by the lack of an apparatus with

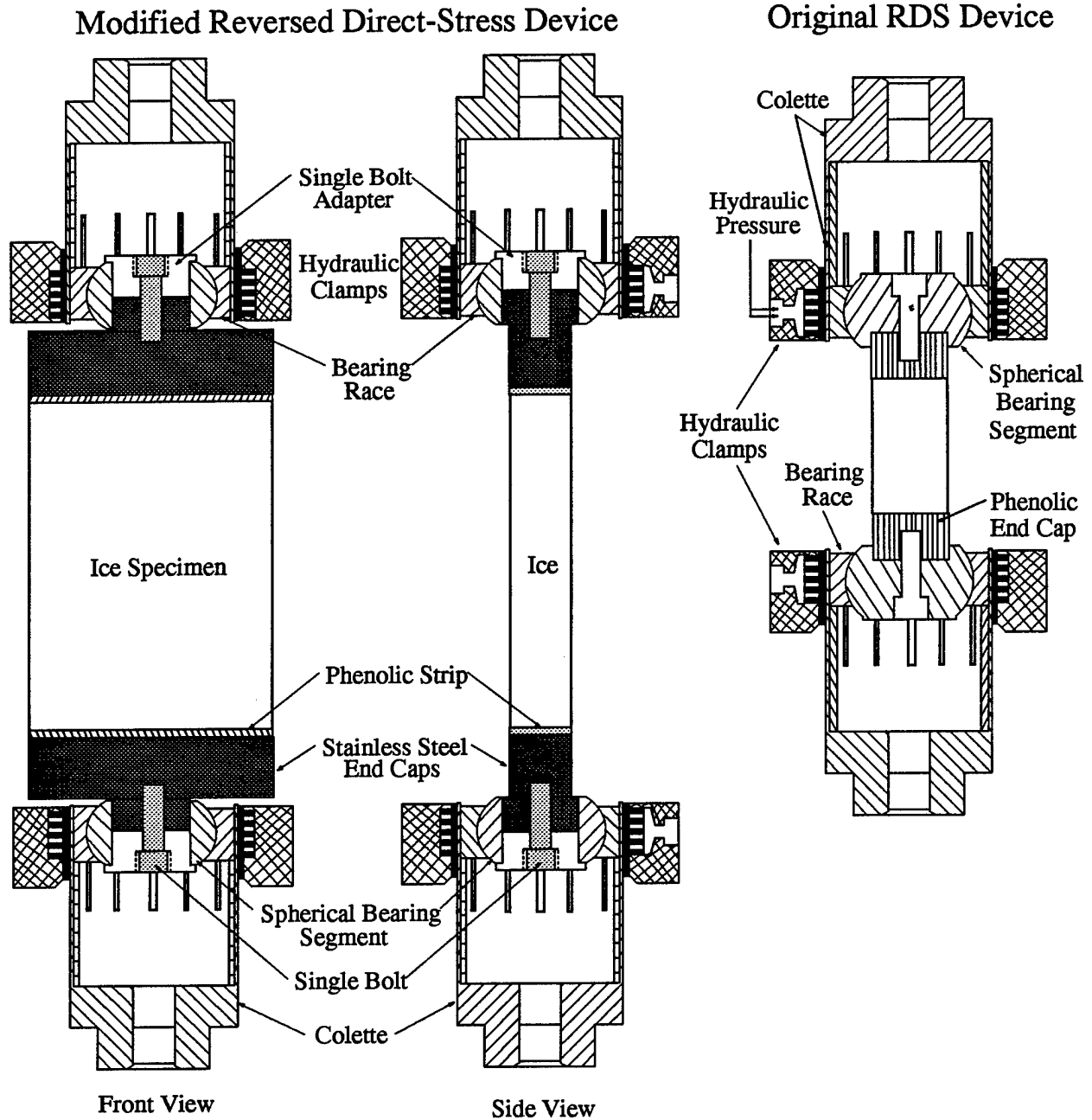


Figure 2.1: Cross-Sectional comparison of the modified reversed direct-stress device and the original RDS device designed by Cole.

these capabilities which could effectively attach an imperfect ice specimen to the load system.

Although this may seem to be a straightforward process, the problem of nonparallel end

planes, and hence specimen misalignment with the load train, makes this a very difficult task.

By using accurate wood-finishing tools such as a planer, bandsaw and milling machine, ice specimens can be manufactured within close tolerances to a desired size and shape. Even with the precision of these tools, the degree of accuracy produced in metal or ceramic specimens can not be produced in ice specimens. Therefore, it is inevitable that the end planes of each ice specimen will be non-parallel or misaligned to some degree. Previous attachment systems have solved this problem by including either universal joints or ball seats in the load train. Although both joint types will effectively solve the end plane misalignment problem, they exhibit two significant limitations.

The primary problem occurs when the specimen is loaded. Neither universal joints nor ball seats can prevent the specimen from rotating and re-orienting itself. This causes the loading axis to shift from its original position, creating a transient stress field. A second problem is the inherent mechanical 'play' in their design. This slack allows the joint to re-orient itself when the specimen transfers from one load regime to another during load reversal. In the transition there is a shift in the load hysteresis loop and a closed-loop hydraulic testing machine may not be able to accurately control the process. The effect of this event is a disruption in the cyclic loading and occasionally it causes the destruction of fragile specimens.

The RDS device circumvents both of these problems by the nature of its design. Using the endcapping procedure detailed later in this paper, the end plane misalignment can be

partially corrected when the end caps are attached to the specimen. Any remaining misalignment is easily accommodated by a spherical ball and race assembly. As the endcapped specimen is loaded into the colettes (see Fig. 2.1a), which are affixed to the crosshead and actuator of the testing machine, the race assembly freely revolves around the ball until it adapts the misaligned specimen to the properly aligned test machine grips. At this point the race is circumferentially clamped to the ball producing a load train which, for symmetrically loaded geometries, is very stiff and develops a uniform stress field. Because the RDS device becomes a rigid system after the specimen is clamped, the problem of mechanical 'play' is avoided. This allows the load actuator to cycle the specimen smoothly between the tension and compression regimes with no loss of control.

2.4 End Cap Modifications

Several modifications have been made which both improve the performance and extend the applications of the original RDS device. The primary design change was motivated by the desire to test square plate geometries rather than cylindrical cores. The original device grips the specimen using a cylindrical phenolic end cap. The end caps are then attached to the test machine via a spherical ball and race assembly which can be hydraulically clamped in any position to accommodate specimen end plane misalignment. To adapt the device for square plate geometries a new end cap was designed to transmit load evenly over a rectangular area, while still utilizing the clamped ball and race assembly.

In order to resist the shear and bending moment forces induced by unsymmetrically extending the end caps beyond the centerline of the load train, it was necessary to increase

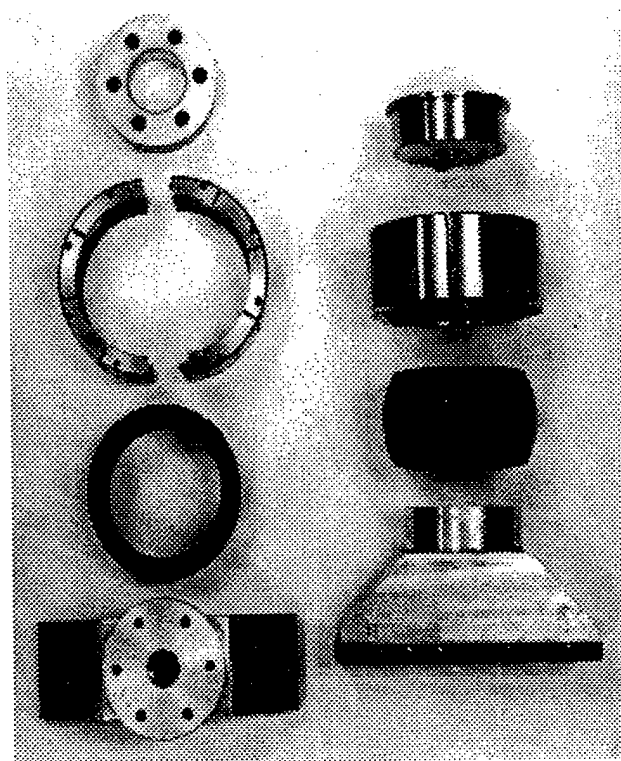


Figure 2.2: The aluminum end cap system. From the top are the multi-bolt adapter, bearing race, spherical bearing segment and the trapezoidal shaped end cap.

the strength of the end cap material. Without some type of metallic backing the phenolic resin would be too flexible to maintain a uniform state of stress. The first set of end caps, depicted in Figure 2.2, were made of aluminum, which made them lightweight, despite their large size. Initially several widths were fabricated, ranging from 15.24 cm to 30.48 cm with each having a thickness of 5.08 cm. The original set also incorporated an adapter system for attaching them to the spherical segment using multiple small bolts around the perimeter in place of the single large bolt in the original system.

In place of the Synthane material used in the original device (Cole and Gould, 1990a) and other tensile testing devices (Currier and Schulson, 1982; Lee, 1986; Richter-Menge and

Jones, 1993), a cotton fiber reinforced phenolic (Grade C Garolite) was used to form the bonding interface between the aluminum and the ice. Using a milling machine, cubes with approximately 1 mm sides were machined in a cross-hatch pattern through several of the alternating resin/fiber reinforcement layers of the phenolic material. This process exposed some of the fiber reinforcement and enhanced the bonding performance of the material, but initial tests (Lazo, 1994) showed that the surface was still not adequate to prevent bond delamination prior to specimen failure. The problem was remedied by roughening the phenolic surface with a wire brush. By doing so more of the fibers were exposed providing a significantly greater surface area for the ice to bond to. After the phenolic material was processed a 1 cm thick strip was epoxied to the aluminum.

Two problems were evident with the new aluminum end caps. First, after repeated usage, the phenolic strip delaminated at the interface between the epoxy and aluminum. To remedy this, machine bolts were used in conjunction with the epoxy resin to re-attach the strip. The second more serious problem was found in the new adapter system. After performing several experiments, discrepancies were found between the displacements measured on each of the end cap's cantilevered sides. It was then determined that if the perimeter bolts of the adapter, which attach the end cap to the spherical segment, were not tightened equally, each side of the end cap could deflect independently, making one side more compliant than the other. Although it could not be accurately measured, it was also suspected that the taper of the aluminum near the cantilevered ends was allowing the end caps to deflect slightly. In order to eliminate any deflections which this may have caused, a new, more rigid set of end

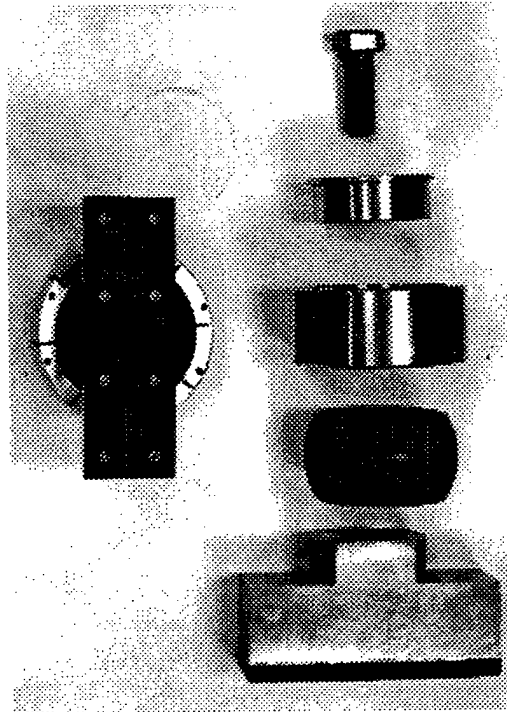


Figure 2.3: The stainless steel end cap system. From the top are the large single bolt, the new adapter, the bearing race, spherical bearing segment and the stainless steel end cap. On the left is the assembled end cap system.

caps was designed.

Three primary modifications were made in the second design, shown in Figure 2.3. First, the material was changed from aluminum to stainless steel. This provided better saline corrosion resistance and more rigidity. Second, the adapter system which required multiple bolts to attach the end cap to the spherical segment was replaced by a system similar to the original which relies on a single, large diameter bolt. This allowed controlled tightening with a torque wrench prior to each experiment. Finally, the lower section of the end cap was changed from a trapezoidal shape to a rectangular shape. This eliminated the tapered cantilever ends which were thought to be inadequate for inhibiting deflection and created a very stiff end cap capable of imposing the desired uniform stress field. Unfortunately, this

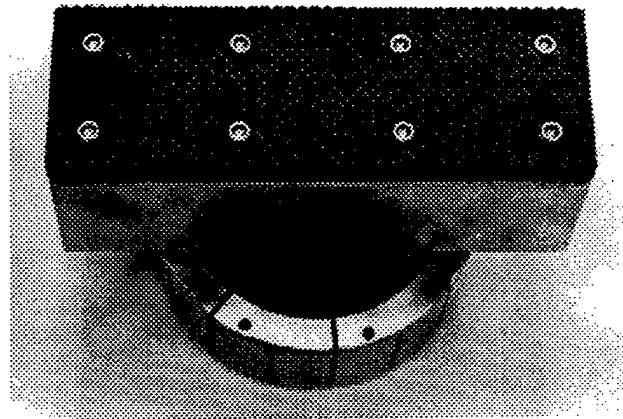


Figure 2.4: A fully assembled stainless steel end cap. The phenolic is attached with both epoxy and bolts due to the strength of the bond which the phenolic's machined surface can create.

also added significantly more weight to the end caps. Due to the extra weight and the cost of machining the stainless steel, only two sizes were fabricated in the second design. One 10.16 cm and one 15.24 cm width end caps, both with a 5.08 cm thickness, were made. The phenolic was again attached to the steel with both epoxy and bolts to avoid the delamination problem discovered with the aluminum end caps. Figure 2.4 shows the configuration of the bolts as well as the texture which was machined into the phenolic to enhance its bonding ability.

2.5 Endcapping Procedure

Prior to each experiment the end caps must be securely bonded to the specimen. A procedure was developed which closely follows those illustrated by Cole et al (1985) and Richter-Menge et al (1993) whereby the specimen was bonded with freshwater to the phenolic surface of the new rectangular end caps. When done correctly this procedure produced a bond with a

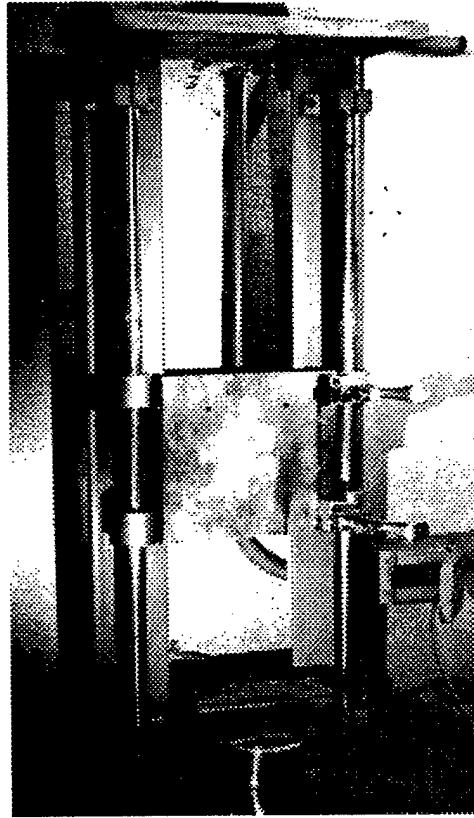


Figure 2.5: The mounting jig used for aligning a specimen with the end caps during the endcapping procedure.

higher tensile strength than the specimen itself, thus allowing the specimen to fracture prior to delamination of the end cap bond.

The first step in the procedure was to rigidly fix the specimen in the desired position for attaching the end caps. For this purpose a special mounting jig (see Fig. 2.5) was fabricated based on the design used by Cole et al (1985). The jig rigidly clamps the specimen to a vertically sliding platform which can be locked in any stationary position above the end cap. With the specimen securely mounted in the jig, the end caps were prepared for the bonding process. First the phenolic surface was thoroughly cleaned and then a strip of duct tape with approximately 1.5 cm of its edge folded over was attached to the sides. This formed

the walls of a reservoir that would hold the freshwater necessary for the bond. When it was attached, great care was taken to insure that the tape adhesive formed a water-tight seal with the steel of the end cap. During the bonding attempts when the seal did leak, voids were created in the bond near the unsealed area of the tape. If this occurred, the specimen was cut free from the end cap with a bandsaw, reshaped, and the process repeated.

Once the reservoir was properly attached and sealed, it was filled with tap water to saturate the phenolic. When the phenolic was fully saturated, the water was removed and the end cap was placed in the cold room where it was positioned at the base of the mounting jig. Here the end cap was aligned so that the specimen could be lowered directly into the confines of the reservoir. The specimen was then raised out of the way so that water could be added to the reservoir again. After the saturated end cap had cooled for a few minutes, freshwater very close to the freezing point was added and allowed to stand until small ice crystals and dendrites formed along the edge of the reservoir. At this point the specimen was slowly lowered until it began to displace some of the water (see Fig. 2.6). When the displaced water reached the top of the reservoir walls, the specimen was clamped in place and then left undisturbed while freezing occurred.

After the first end cap bond had solidified, the specimen was removed from the jig, turned upside down and remounted in the jig so that the second end cap could be attached using the same process. When the second end cap bond had solidified, the specimen was released from the jig and the tape reservoirs were removed. The end cap bonds were then carefully inspected to determine that there were no air voids. If any were found, the ice was cut free

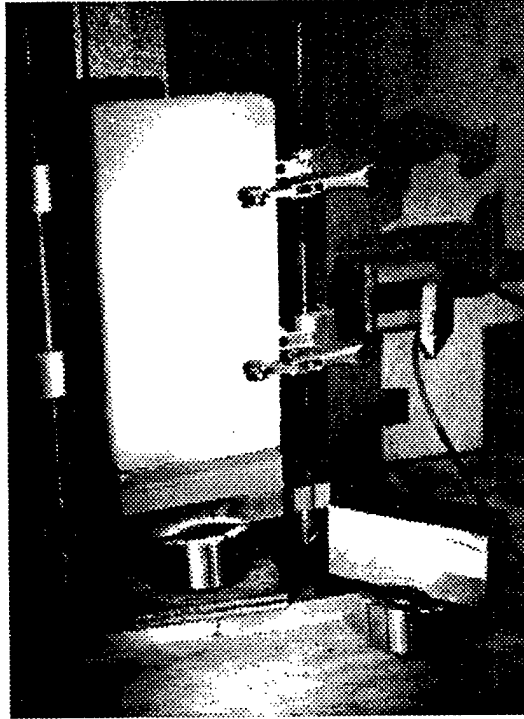


Figure 2.6: A specimen which has been lowered into the water filled reservoir. The second end cap, with its reservoir already prepared, is next to the jig.

from the end cap, reshaped, and the process repeated. If none were present, the endcapping procedure was complete.

2.6 Experimental Results

With the modifications presented here the RDS device can be used to test a variety of tensile specimen loading geometries. The first published set of experiments performed with an initial version of the modified RDS device utilized the specially developed short rod Chevron Notched Tension (CNT) geometry (Stehn et al, 1994). In that study, CNT specimens were used to measure the fracture resistance of large-grained S1 freshwater ice. Stable *stick-slip* crack growth was also developed, in part, due to the high rigidity of the RDS system.

The most common geometry tested with the RDS is the square plate/pure tension spec-

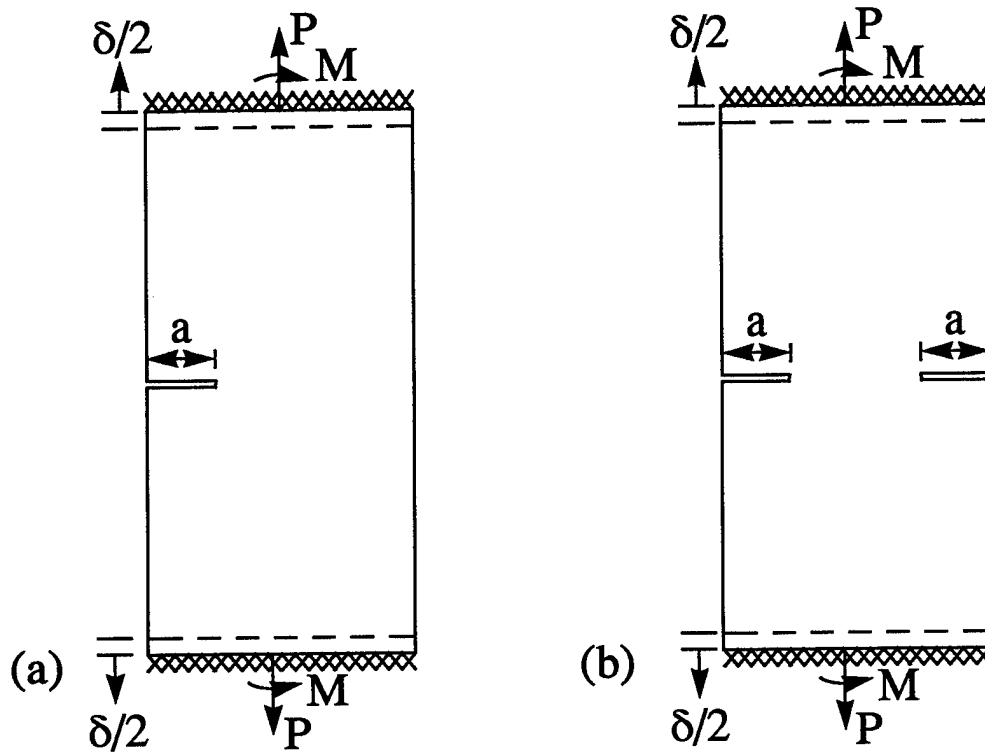


Figure 2.7: (a) The Single Edge Notch (SENC) and (b) Double Edge Notch Clamped Strip (DENCS) geometries.

imen. Recent testing has focused on this basic geometry, as well as the Single Edge Notch Clamped Strip (SENC) and Double Edge Notch Clamped Strip (DENCS) fracture variations (see Fig. 2.7), with typical loading consisting of a series of monotonic tensile ramps, followed by creep recovery sequences and finally a ramp to failure. In most cases the loads are applied with the actuator in load control. For the monotonic series the load is linearly ramped from zero to approximately 30% of the predicted tensile capacity and then immediately removed. This process is then repeated over a range of loading rates, each time reaching the same peak before unloading. The creep recovery sequences consist of three constant loads separated by periods of unloading during which the specimen is allowed to

'recover' the induced elastic and anelastic strains. As the sequence progresses both the loading and unloading times are proportionally increased. When the final unloading period is complete, the load level is increased and the sequence begins again. Typically this process is repeated for three load levels. Using load and displacement data from these types of tests, elastic and viscoelastic properties can be measured.

To date, ten specimens have been successfully tested using the modified tension device. Three other specimens failed prior to completion of the tests. In two cases, the end cap bond failed and in the other case the phenolic strip delaminated from the aluminum portion of the end cap when the epoxy bond failed. Since the size of the end caps was fixed, all of the specimens were 15.24 cm wide and 5.08 cm thick. In order to achieve a 2:1 length to width ratio, the specimens have all been 30.48 cm in length. Each test strip was machined such that the failure plane would occur perpendicular to the surface of the ice sheet, which is consistent with failure due to the in-plane tensile forces found in naturally occurring ice sheets. Although all of the specimens were machined from ice grown under the same conditions, they were not all harvested from the same parent sheet. Since this may cause some variation in the test results, only the information concerning the four square plate/pure tension specimens cut from the same parent sheet has been included in this paper.

All of the specimens tested were composed of lab grown S2 saline ice. The ice growth process began with the mixture of tap water and granulated agricultural salt to create a brine solution. The two components were combined in a 1.2 m³ basin until the mixture reached a salinity of 26 ppt. The temperature of the solution was then lowered to between

0 and -1°C by circulating the brine through the -25°C air with a miniature sump pump. When the solution reached the appropriate temperature, the ice was seeded by spraying a fine mist of the brine solution over the surface under quiescent conditions. After a visible seed layer of ice crystals had formed, the basin was allowed to stand undisturbed during the growth of the ice sheet.

The ice was harvested after one week when it had grown to approximately 30 cm in thickness. It was then stored as smaller blocks in the same cold room at -23°C until it could be machined into test strips. When test strips were needed, several were made using a chainsaw, bandsaw and benchtop planer and then stored in a chest freezer at -27°C . The final step in making the finished specimens was the endcapping procedure which was performed at -15°C . When the endcapping was complete the specimen was placed back in the -27°C chest freezer until testing began, typically less than one week later. On the day prior to the experiment the specimen was moved to the testing cold chamber to acclimate to the desired -15°C test temperature.

On the test date the specimen was carefully placed in the collets which were already mounted in a closed-loop, servo-hydraulic testing machine (Instron 8502). When the spherical segments were properly seated to allow for the end cap position, the specimen was clamped in place with the hydraulic circumferential clamps.

2.6.1 Data Acquisition and Reduction

For experiment T1221, the displacement was measured over the central 20 cm of the specimen using two non-contacting KAMAN gauges (measuring range $\pm 250\text{ }\mu\text{m}$), with one mounted

on each of the 5 cm faces. Experiments T131 and T201 utilized the same 20 cm gage length, but used four LVDT's (measuring range 500 μm) to measure the displacement. The failure ramps of the previous three experiments were all performed in load control. The fourth experiment, T302, again utilized the four LVDT's, however, two were attached to the ice over a 26 cm gage length and the other two were attached to the steel end caps with an effective gage length of 30.5 cm. The failure ramp for specimen T302 was performed with the actuator in strain control using the feedback from one of the four LVDT's.

The load and displacement data for each experiment was recorded in triplicate using three individual acquisition systems. The primary system was a Sheldon Instruments digital recorder which sampled at low to mid range frequencies of 1 to 1000 Hz, and then stored the data on a Tangent 486/33 personal computer. The secondary system was a high speed SONY digital tape recorder which was used to record details of the failure at 5000 Hz. As backup to the first two systems, data was also recorded at 10 Hz on a Gateway 486/33 PC using VIEWDAC data acquisition software. This same software was also used to monitor each channel simultaneously in real time.

Following each test the relevant portions of the data were extracted from the records and smoothed by fitting polynomial functions to them as shown in Figure 2.8a. A single Strain vs. Time plot was then developed for each loading by averaging the smoothed curves of each displacement gauge. Finally, the averaged strain was used with the smoothed stress vs. time curve to create the Stress vs. Strain plot used to determine the moduli.

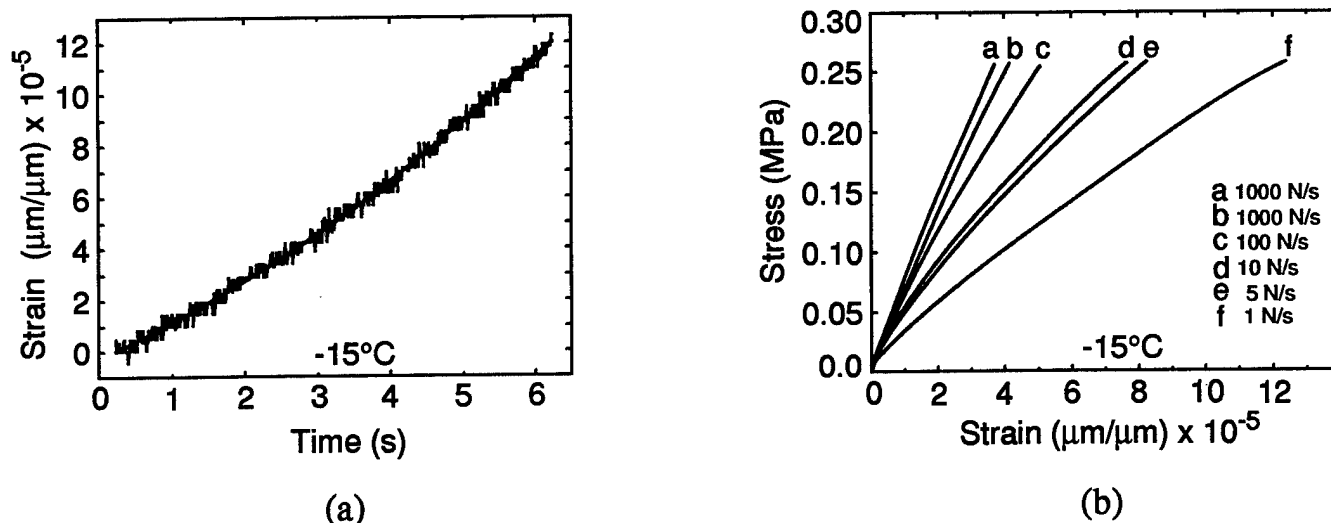


Figure 2.8: (a) The polynomial curve fit of a displacement vs. time plot obtained from an LVDT during experiment T201. (b) Stress vs. Strain curves for monotonic loading from 0 – 2000 Newtons at loading rates between 1 to 1000 N/sec.

2.6.2 Monotonic Ramp Tests

All four of the square plate/pure tension specimens were subjected to monotonic ramp loadings. The peak load for each test was constant at 2000 Newtons (approximately 0.26 MPa) which corresponds to about 30% of the expected tensile failure load (stress). This load was chosen because it produced easily measurable elastic and anelastic strains, but produced no significant viscous strain. The load was applied at consecutive rates of 1000, 100, 10, 5 and 1 N/s, and then again at 1000 N/s for specimens T131, T201 and T302. Specimen T1221 was tested at the same rates except for the 5 N/s and the second 1000 N/s loading. Unloading occurred at 1000 N/s for all of the ramps on each of the specimens.

When all of the monotonic ramp tests were complete, one final ramp to failure was imposed on the specimens. Based on an expected failure load of approximately 6 kN, the loading rate for the tests under load control was set at 1000 N/s, giving a time to failure of

Table 2.1: Uniaxial tension test results

Specimen Name	Salinity ppt	Density Mg/m^3	Temp. $^{\circ}\text{C}$	Control	Rate	E_i GPa	E_f GPa	σ_f MPa
T1221	5.25	0.891	-15	LOAD	1000 N/s	3.4	1.7	0.7
T131	6.35	0.893	-15	LOAD	1000 N/s	7.1	5.7	0.85
T201	6.64	0.920	-15	LOAD	1000 N/s	6.6	4.0	0.77
T302	6.5	0.897	-15	STRAIN	5 $\mu\text{m/s}$	6.1	3.0	0.67

approximately six seconds. This rate was chosen so that the resulting stress vs. strain curves would be nearly linear, but also have a reasonable time duration for the data acquisition systems to record information. For the final ramp of experiment T302, the loading was performed in displacement control at a rate of 5 $\mu\text{m/s}$.

Figure 2.8b shows the Stress vs. Strain plots generated by the data from experiment T302. It clearly shows the direct relationship between loading rate and modulus: As loading rate decreases, both the initial (E_i) and final modulus (E_f) decrease. Values of the initial modulus range from 7.4 GPa for the fastest ramp (1000 N/s), to 2.8 GPa for the slowest ramp (1 N/s) (see Table 1). As expected, the final modulus was lower than the initial, ranging from 6.4 to 1.5 GPa, for the 1000 and 1 N/s ramps, respectively. Another interesting characteristic which seemed to develop was a stress history effect. Comparing the two 1000 N/s ramps, there is a measurable decrease in the moduli by 0.5 and 1 GPa for the initial and final, respectively. The second ramp, which was performed after the lower ramp frequencies were completed, shows an increase in specimen compliance which is directly attributed to the prior loadings. Visual observations of the specimen during each experiment revealed no evidence

of microcracking damage.

2.7 Summary

The RDS device has proven to be a very adaptable system for uniaxial stress testing. With the modifications outlined here it is now possible to apply a constant, reversible stress field to square plate specimens. Due to the device's ability to rigidly clamp the aligned specimen in place, there is no mechanical 'play' or slack in the system, allowing smooth tensile load initiation and transition between tensile and compressive regimes.

Several improvements were made in the modified end caps. The new phenolic material (Garolite) with its roughened, machined surface has proven to be very effective as a bonding surface. Of the thirteen specimens which were tested, only two failed within the freshwater bond area during an experiment. This success rate has been very encouraging, particularly when considering that the two failures occurred during the initial development of the bonding procedure. While the basic procedures developed by Cole et al (1985) and Richter-Menge et al (1993) for endcapping core specimens are still used, a new reservoir system was devised to produce a bond between the specimen and the rectangular end caps.

The modified end caps have been extended beyond the central, supported region of the device. In order to maintain a constant stress field across their width, they must be capable of resisting shear and bending forces, in addition to the applied axial forces. Since the phenolic was too flexible for this purpose, a combination metal/phenolic end cap was devised. The first version consisted of an aluminum body with the phenolic layer attached with epoxy. Due to problems with the shape of the aluminum body and the eventual delamination of

the epoxy bond, a second set was designed utilizing stainless steel. To avoid the deflection problems induced by the shape of the aluminum body, the stainless steel was machined in a solid rectangular shape. The delamination problem was eliminated by attaching the phenolic with both epoxy and bolts.

Initial experimental results with the RDS device have been very encouraging. Values of the failure strength and moduli obtained from monotonic ramp tests agree well with those found in the literature (Cole, 1990b; Richter-Menge and Jones, 1993; Cole and Durell, 1995a). To date, the device has been primarily used for tensile strength and fracture experiments, but future testing will make use of its reversible loading abilities.

2.8 Future Research

Current research with the RDS device is focused on the constitutive and fracture properties of first year sea ice. During Phase 6 of the Sea Ice Mechanics Initiative (SIMI) project several full sheet depth core ice samples were collected near Barrow, Alaska in May of 1994. These cores were subsequently shipped back to Clarkson University, where lab scale tests will be performed in an attempt to correlate the findings of the field scale experiments (Adamson et al, 1995) with lab scale results. Of primary interest is the constitutive information obtained from various cyclic loadings applied in the field, which will be reproduced with the RDS device. Observations made in the field determined that the ice cover in the testing area had a very strong c-axis alignment. The effects of this strong alignment on the fracture properties will also be examined using the Single Edge Notched Clamped Strip (SENCs) specimen geometry. Ultimately, results from both testing programs will be used to develop

a constitutive model for first year sea ice (Cole and Durell, 1995a; Cole, 1995b; Mulmule et al, 1995). Future research will include a finite element analysis of the SENCs geometry which will determine the appropriate limits for the length to width ratio.

3 CORE-BASED FRACTURE (PHASE VI) OF ALIGNED FIRST YEAR SEA ICE²

3.1 Abstract

In conjunction with Phase VI of the large scale in-situ fracture test program undertaken during the ONR Sea Ice Mechanics Initiative (SIMI) project, three full depth cores were collected from the first year sea ice sheet near Pt. Barrow, Alaska and shipped back to Clarkson University for further analysis. A detailed study of the ice fabric (Cole et al, 1995) at the site revealed that there was a very strong horizontal c-axis alignment. With this in mind, a set of fracture experiments utilizing the Semi-Circular Bend (SCB) fracture geometry was developed to determine the effects of the alignment on the apparent fracture toughness, K_Q . The effect of crack orientation with respect to the basal plane on K_Q was also investigated by initiating fracture either parallel or perpendicular to it. To match the field conditions at the ice surface, the tests were performed isothermally at -10°C . Using closed-form solutions presented in Adamson et al (1996) for the SCB fracture geometry, values for K_Q were determined directly from load and displacement data. Results show that there is a slight, but recognizable decrease in fracture toughness as depth and c-axis alignment increase. Crack orientation has a more noticeable effect, with fracture toughness being measurably lower when the crack path follows the basal plane. Overall, the results compare well with other small-scale experiments performed on ice with similar characteristics and temperature.

³Accepted for publication in *ASCE Journal of Cold Regions Engineering*, August 1996.

3.2 Introduction

In May of 1994, Phase VI of the large scale in-situ fracture test program undertaken as part of the Sea Ice Mechanics Initiative (SIMI) project was completed near Pt. Barrow, Alaska. One of the objectives of this project was to examine the scale effect on the fracture properties of sea ice. To this end, specimens were tested in-situ over a size range of 1:120 (Adamson et al, 1995). In conjunction with the large-scale program, previous Phases of the SIMI project had included a number of small-scale experiments which served to correlate the large-scale information concerning first year sea ice with current lab-scale data available in the literature.

Since a very limited amount of time was available during this phase to complete the large scale tests, there was insufficient time to perform the corresponding small-scale tests in the field. To follow the precedent set in previous phases of recording small and large-scale fracture data for ice which grew in the same field location, three full depth cores were harvested at the field site in Elson Lagoon and sent to Clarkson University to complete the small-scale testing. This paper describes the first segment of fracture testing performed on one of the cores utilizing the SCB fracture geometry.

Due to the presence of tidal currents in Elson Lagoon, the ice sheet developed with a very strong c-axis alignment through the depth of the sheet. This alignment was so evident at the field site that the direction of the basal plane could be visually determined from the tidal cracks present at the ice surface. Therefore, of primary interest for this study is the effect of the strong c-axis alignment on the apparent fracture toughness, K_Q , and the modulus of

elasticity, E' . The effects of fracture plane orientation with respect to the basal plane on K_Q and E' will also be examined.

3.3 Background

Over the past two decades researchers have been gathering experimental information on the fracture toughness of sea ice at both laboratory and field scale. Among the authors on this topic are Vaudrey (1977), Urabe et al (1980), Shapiro et al (1981), Urabe et al (1981a,b), Timco and Frederking (1982), Shen and Lin (1986), Parsons et al (1986), Urabe et al (1986), Tuhkuri (1987), Bentley (1992), DeFranco and Dempsey (1992), Williams et al (1993), DeFranco et al (1994) and Lazo (1994). A collective history of the experimental information provided by each author has been compiled in Adamson et al (1995). These studies focus primarily on the effects of loading rate, crack orientation, grain size, specimen size, temperature, brine volume and salinity on the apparent fracture toughness. Although these factors have been thoroughly proven to cause significant variations in K_Q , there is another that is often overlooked which can have a measurable influence: crystal orientation or c-axis alignment.

Of the previous articles written on the fracture toughness of sea ice, only a few contain details of the ice fabric beyond the average grain size. In Shapiro et al (1981) there is some discussion regarding the average c-axis direction and its fluctuation with depth. However, there is no quantitative data included from which the degree of alignment can be concluded, nor is there any attempt made to compare c-axis alignment and K_Q . Timco and Frederking (1982) included detailed measurements of fracture toughness versus depth and brine volume,

as well as providing thin-section micrographs of the ice through the depth of the sheet. Unfortunately, there was also apparently no attempt made to compare K_Q with the developing c-axis alignment through the depth.

One of the major factors thought to influence the fracture behavior of the Pt. Barrow ice sheet was the c-axis alignment. Examination of the ice fabric at the site (Cole et al, 1995) determined that a very strong horizontal c-axis alignment developed through the sheet. Such strong crystal alignments have been shown (Weeks and Gow, 1979) to be caused by tidal currents present during the formation of the ice sheet. As part of the SIMI research project at Pt. Barrow, Shapiro and Weeks (1995) examined the effects of c-axis alignment on the flexural strength of small beam samples. Their results indicated that the strong alignment, coupled with brine-drainage networks, played a significant role in the flexural strength of the beams.

As noted above, several previous phases of the SIMI project have included a corresponding small scale testing program. Due to the ease of collection and the minimum amount of handling necessary for testing ice cores, most of the small scale tests have utilized some form of core-based specimen geometry. The geometry selected by the authors for Phases III, IV and VI was the Semi-Circular Bend (SCB), which has the advantage of creating two times the number of specimens from a single core as most other core-based geometries. First developed by Chong et al (1984) for use in rock mechanics research, the SCB has since been rigorously characterized by Adamson et al (1996) using the weight function method. By that solution, the fracture toughness can be determined directly from the load and crack mouth

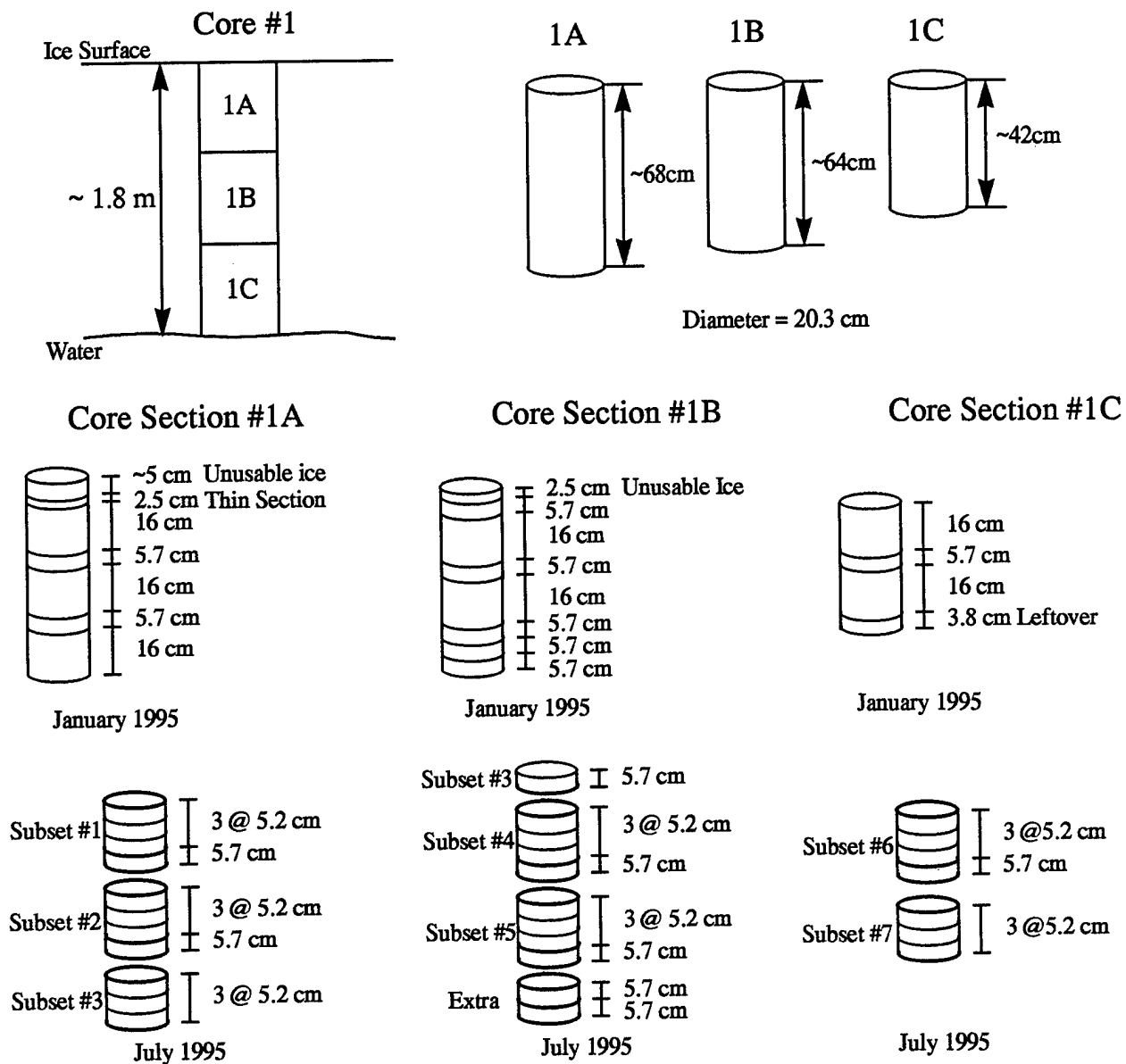


Figure 3.1: The processing history of Core #1 from harvest to disc form.

opening displacement (δ_{CMOD}) at failure.

3.4 Experimental Program

All of the specimens used in this study were cut from a single full-depth ice core that was harvested in May, 1994 from the Elson Lagoon near Pt. Barrow, Alaska. The core was

removed from the 1.8 meter thick floating ice sheet using a 20.3 cm diameter coring auger. Due to the length of the auger barrel, the core was removed in three sections which were approximately 68 cm, 64 cm, and 42 cm, respectively. The core sections were wrapped in plastic and packed with snow in an insulated container for shipment back to Clarkson University.

Upon arrival the core sections were immediately removed from the shipping container and placed in a chest freezer for storage at -27°C . After seven months they were cut with a bandsaw into alternating 16 and 5.7 cm thick disks, which were to be used for SCB and square plate Reversed-Direct-Stress (RDS) specimens, respectively. Later, a change in the testing plan led to cutting the 16 cm disks into thirds and then storing them for another seven months under the previous conditions.

In order to test both SCB and square plate RDS geometries from approximately the same level in the ice core, four disks in sequential order were used to make the final specimens for each subset of tests. The two disks closest to the surface of the original ice sheet in each subset were used to form the SCB specimens. The third and fourth disks of each subset were used to form square plate RDS specimens. Using this partitioning system, six full subsets, each containing four disks, and a seventh containing three disks were created from the full depth core. This provided specimens for two different test geometries at precise intervals through the depth of the ice sheet. Figure 3.1 shows the progression of the ice from raw core sections to the finished specimens. Results from the RDS testing program will be published in a separate article.

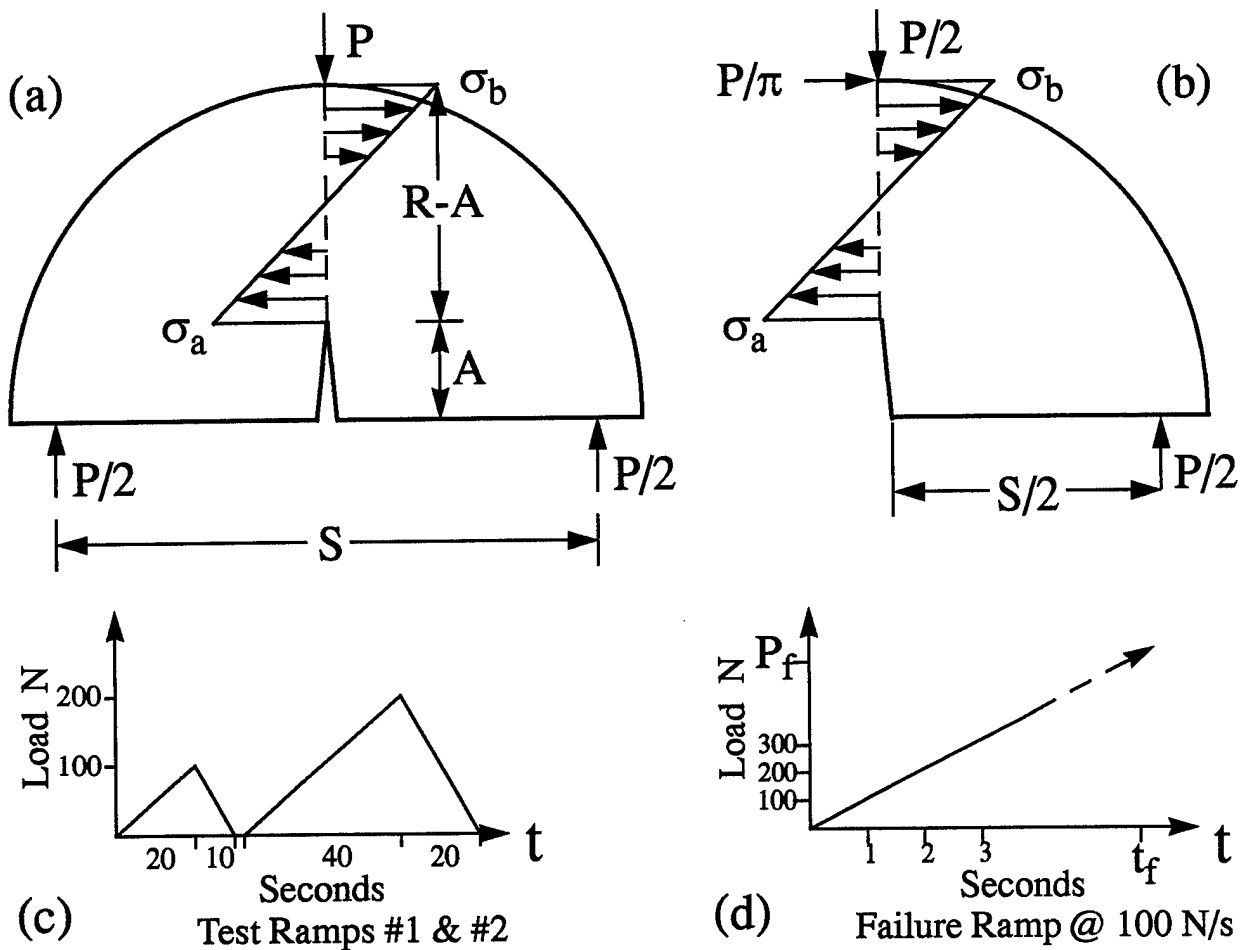


Figure 3.2: The SCB's were loaded in 3 point bending (a) with a load-controlled, linear ramp (c) until fracture occurred.

3.5 SCB Preparation and Setup

Each of the upper two disks in every subset were used to produce two SCB fracture specimens. The first disk was cut in half perpendicular to the basal plane to create specimens for fracture along that plane in the "easy-fail" direction and were designated as FR1AE and FR1BE. The second disk was halved parallel to the basal plane to create specimens for fracture perpendicular to that plane in the "hard-fail" direction and were designated as FR1AH and

FR1BH. This nomenclature was continued through the depth, with the letters E and H indicating easy or hard fail crack propagation, the numerals indicating increasing depth in the sheet and A & B indicating the two specimens cut from each individual disk. After each disk was cut in half with a bandsaw, a benchtop planer was used to machine a flat, smooth surface on the bottom of the SCB and also to create a small flat surface at the top for use as the point of bearing for the center load support. The specimens had a final radius of approximately 9.8 cm and a thickness of approximately 5 cm. When complete, the specimens were labeled and triple-bagged in plastic for storage at -27°C to await the testing procedure.

All of the experiments were performed at a temperature of -10°C , regardless of the original depth of the specimen within the sheet. This temperature was chosen to correspond with the field conditions present at the ice surface during Phase VI. Although this temperature is appropriate for the SCB's taken from the top of the sheet, the authors acknowledge that the specimens cut from the lower portions of the sheet would in actuality have temperatures approaching -1.8°C . Since the conditions necessary for shipment and storage preclude the ability to maintain the natural temperature profile of the sea ice, no attempt was made to reproduce the original depth-temperature distribution. Instead, the focus of the experiments was centered on the effects of the fabric alignment, rather than the temperature, on the fracture toughness of the ice.

On the day prior to testing the specimens were moved from storage into the -10°C testing cold chamber. Here they were kept overnight surrounded by scrap ice in an insulated

chest to slowly warm to the higher temperature. On the test date, one specimen at a time was removed from the insulated chest and prepared for testing. First, a 2.8 cm crack was cut at the center of the bottom loading surface with a fine-toothed bandsaw and then sharpened with a razor blade. After the crack was prepared, one LVDT gage (Sensotec PLVX/500, measuring range $1000 \pm 0.5\mu\text{m}$) was attached to each side of the specimen at the crack tip with a combination of small screws and freezing water. To measure the crack-mouth-opening-displacement (δ_{CMOD}), an extensometer (Instron 2620-826, measuring range $5000 \pm 1\mu\text{m}$) was frozen across the crack mouth at the center of the SCB. Once the gages were securely attached, the instrumented specimen was placed on the three point bend loading supports where the LVDT gages were zeroed.

Since load history effects on the SCBs' failure strength were not a consideration in this study, the SCB's were simply loaded via a load controlled monotonic ramp at 100 N/s ($\dot{K} \approx 15 \text{ kPa}\sqrt{\text{ms}}^{-1}$) until failure occurred. The only other loadings applied to the specimen were two double-sloped ramps at very low loads (compared to failure) which insured that each of the displacement gages were properly attached and functioning prior to the failure ramp. Figure 3.2 depicts the three point bend loading scheme for the SCB specimens and an idealized representation of each loading ramp. The actual load ramps, as recorded by the primary digital data acquisition system (@ 1 kHz) for specimens FR1AE and FR1AH are shown in Figures 3.3a & c, respectively. The nonlinearity at the beginning of Figure 3.3c was a result of the initial seating of the loading system's roller supports. Also depicted in Figures 3.3b & d are the crack opening displacements (COD) recorded for each test. With

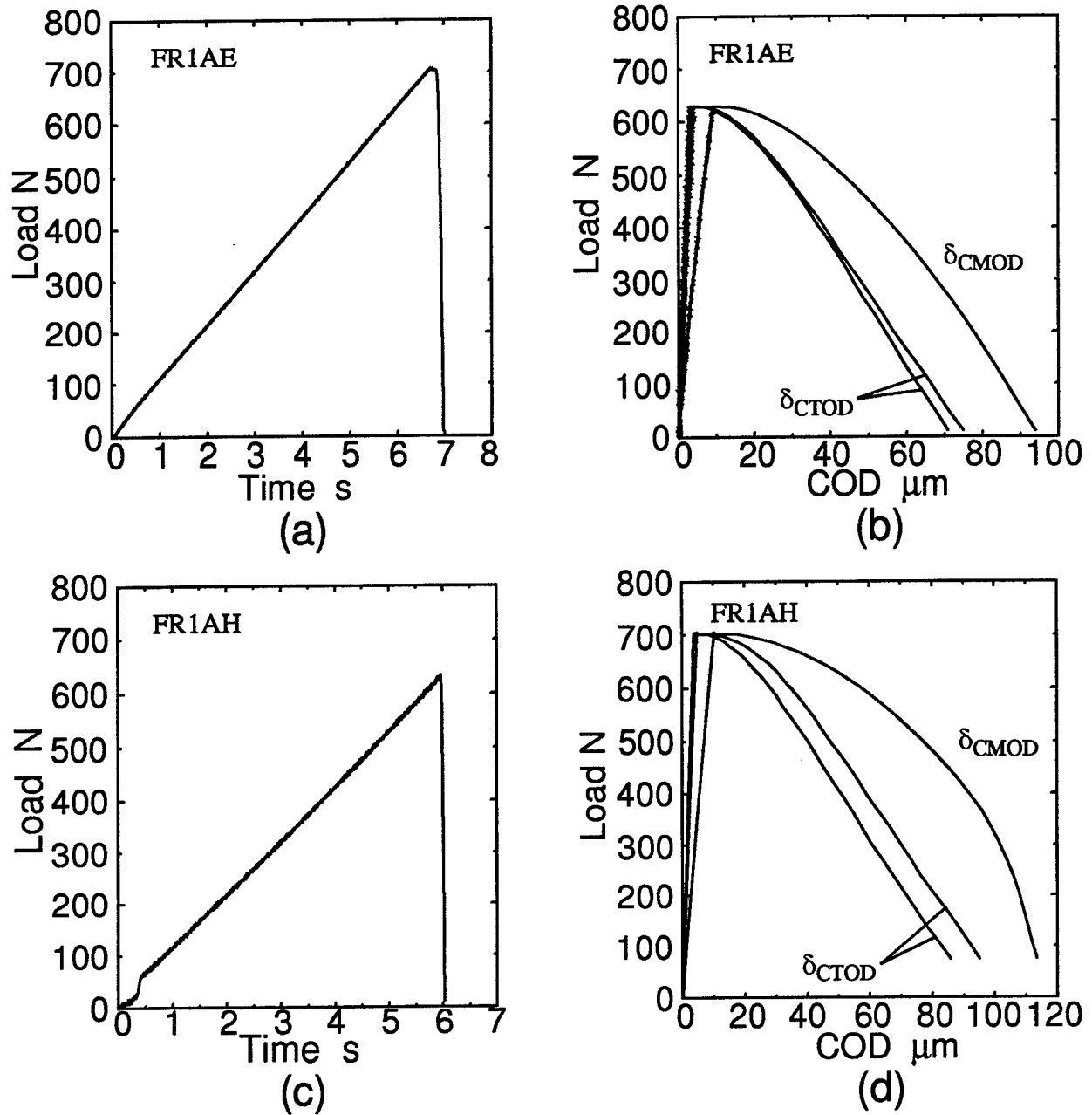


Figure 3.3: Load vs time (a & c) and load vs crack-opening-displacement (b & d) plots obtained from specimens FR1AE and FR1AH.

the use of a secondary high speed (24 kHz) data acquisition system, the unloading portion of each test was also captured. The latter information was used during the post-test analysis to perform a psuedo-fracture energy calculation

3.6 Experimental Results

Of the original 28 SCB specimens cut from core #1, 26 were successfully tested. The two remaining specimens were prematurely damaged due to improper handling and could not be used for testing. The apparent fracture toughness and modulus of elasticity of each specimen were determined with the analytical expressions available in Section 5 of Adamson et al (1996) for the SCB fracture geometry. Based on the peak load at failure (P_f), crack length (A) and $A/R = a = 0.3$,

$$K_Q = 2.36 \frac{P_f}{B\sqrt{R}} \quad , \quad E' = 5.08 \frac{P}{B\delta_{CMOD}} \quad (1)$$

where B is the thickness and δ_{CMOD} is the crack-mouth-opening-displacement.

In addition to K_Q and E' , the nominal tensile failure strength was also determined. As shown in Figure 3.2a, the stress field along the uncracked ligament due to the applied load P was assumed to have a simple linear distribution between the crack tip and the load application point. Solving the equations of equilibrium for half the SCB geometry (see Fig 3.2b), the stresses σ_a and σ_b , for an arbitrary crack length to radius ratio, a , and span, S are:

$$\sigma_a = \frac{P}{BR} \left\{ \frac{\left[\frac{3}{2} \frac{S}{R} - \frac{2}{\pi} \right] + \frac{2}{\pi} a}{(1-a)^2} \right\} \quad (2)$$

$$\sigma_b = \frac{P}{BR} \left\{ \frac{\left[\frac{3}{2} \frac{S}{R} - \frac{4}{\pi} \right] + \frac{4}{\pi} a}{(1-a)^2} \right\} \quad (3)$$

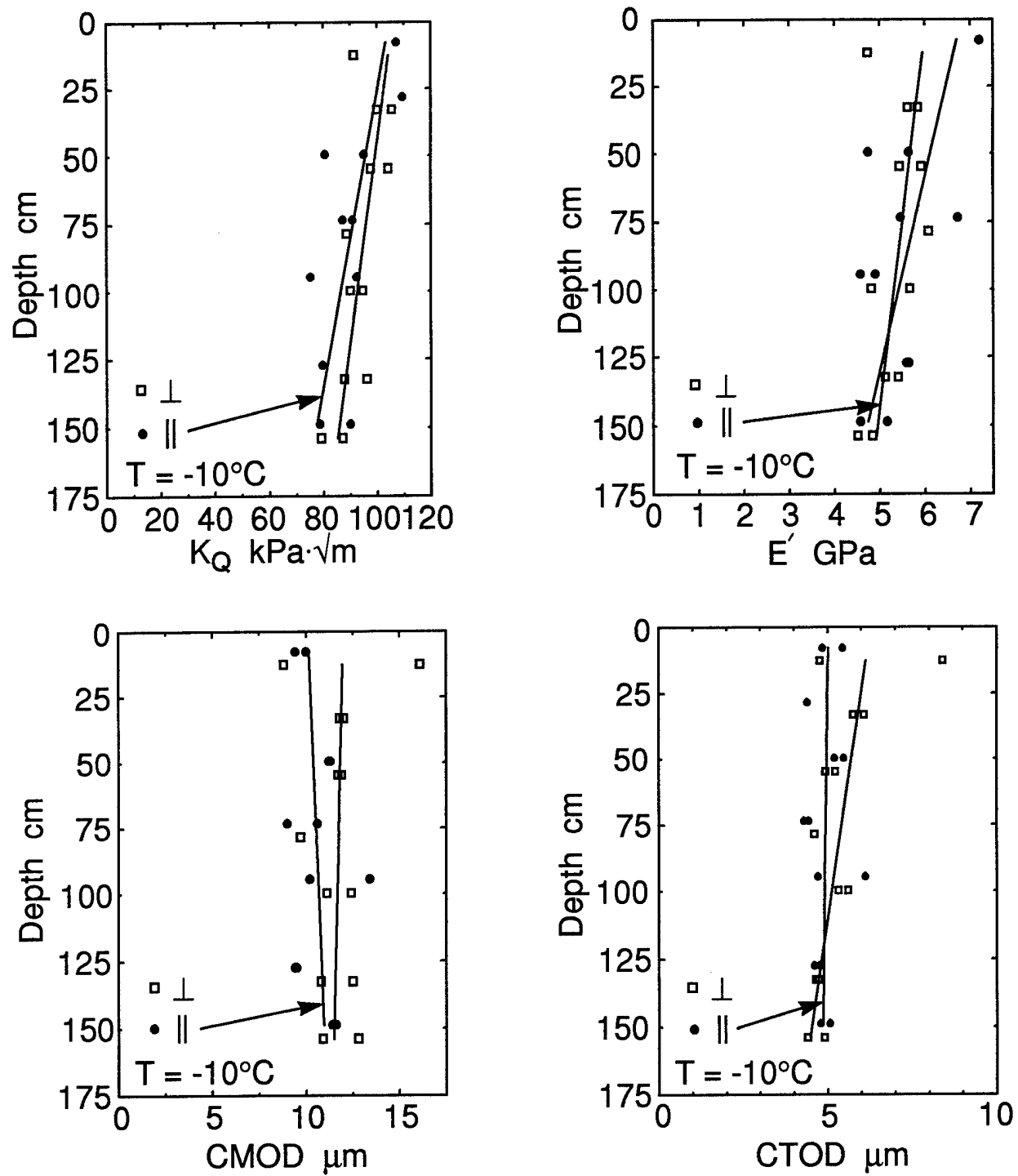


Figure 3.4: K_Q , E' , δ_{CMOD} and δ_{CTOD} vs depth. \perp and \parallel indicate crack propagation perpendicular and parallel to the basal plane, respectively. Each solid line is a linear best fit to the corresponding dataset.

The nominal tensile strength (σ_n^t) of each SCB test was estimated from the magnitude of σ_a at peak load. Given that the dimensions for these experiments were $S = 1.6R$ and $a = 0.3$, it follows from (2) that

$$\sigma_n^t = 4 \frac{P_f}{BR} \quad (4)$$

The results of all 26 tests analyzed using the above expressions are given in Tables 3.1 & 3.2. For clarity, the variation of K_Q , E' , δ_{CMOD} and δ_{CTOD} vs depth through the ice sheet has been shown in Figure 3.4. In each graph, a linear best fit has also been overlayed to accentuate the trend of each quantity through the depth.

From these results, the effect of the crack path orientation with respect to the basal plane can be clearly seen. The apparent fracture toughness (K_Q) values are consistently lower for the specimens which fractured parallel to the basal plane and averaged $90.4 \text{ kPa}\sqrt{\text{m}}$. This result agrees with expectations, since the pre-crack notch channeled the failure crack path along the weakest failure plane of the crystalline structure. For the specimens where the crack was initiated perpendicular to the basal plane, the average fracture toughness is approximately 5% higher at $95.2 \text{ kPa}\sqrt{\text{m}}$. With the only variation between specimens cut from the same depth coming from the failure plane direction, this difference is directly attributed to the weakness of the basal plane. Unfortunately, due to the relatively low number of specimens and the scatter in the data, it is difficult to determine if the increase in crystal alignment with depth caused an increase in the separation between the hard/easy fail direction fracture toughness.

Table 3.1: SCB easy fail fracture test results

Specimen Name	Depth cm	Load N	δ_{CMOD} μm	δ_{CTOD} μm	K $\text{kPa}\sqrt{\text{m}}\text{s}^{-1}$	K_Q $\text{kPa}\sqrt{\text{m}}$	σ_n^t MPa	E' GPa
FR1AE	7.6	718	10.0	5.98, 4.90	15.4	108.4	0.60	7.2
FR1BE	7.6	718	9.4	5.26, 4.46	15.3	107.1	0.59	7.6
FR2AE	—	—	—	—	—	—	—	—
FR2BE	28.2	645	—	4.08, 4.71	17.3	109.4	0.60	—
FR3AE	49.5	562	11.3	5.21, 5.74	14.7	80.7	0.44	4.7
FR3BE	49.5	662	11.2	4.18, 6.24	14.7	95.1	0.52	5.6
FR4AE	73.3	608	9.0	4.59, 4.28	15.3	90.9	0.50	6.7
FR4BE	73.3	583	10.6	4.97, 3.65	15.3	87.2	0.48	5.5
FR5AE	94.6	519	10.2	4.09, 5.33	14.8	75.3	0.41	4.9
FR5BE	94.6	637	13.4	5.93, 6.28	14.8	92.3	0.51	4.6
FR6AE	127.3	526	9.5	3.98, 5.24	15.5	79.7	0.44	5.6
FR6BE	127.3	526	9.4	3.66, 5.86	15.5	79.7	0.44	5.6
FR7AE	148.6	532	11.4	5.50, 4.63	15.1	78.7	0.43	4.6
FR7BE	148.6	608	11.6	5.20, 4.38	15.1	90.1	0.49	5.2

Upon completion of the fracture testing program, the grain structure was examined using a Rigsby stage according to the procedures in Langway (1958). To evaluate the ice in this manner, portions of the specimens of interest were trimmed to size, affixed on a glass slide and then planed down with a standard microtome until they reach approximately 1 mm or less in thickness. By passing the resulting ‘thin section’ between the crossed polarizing plates of the stage, the grain boundaries could be easily observed. Although this technique also allows a thorough investigation of all aspects of the microstructure, the evaluation in this study was limited to the crystal alignment. Information concerning grain size and platelet spacing for ice collected during the same field trip, and in the same location, has previously been presented in Cole et al (1995). In that study, the grain size was found to steadily increase

Table 3.2: SCB hard fail fracture test results

Specimen Name	Depth cm	Load N	δ_{CMOD} μm	δ_{CTOD} μm	K $\text{kPa}\sqrt{\text{m}}\text{s}^{-1}$	K_Q $\text{kPa}\sqrt{\text{m}}$	σ_n^t MPa	E' GPa
FR1AH	12.5	645	8.8	4.25, 5.29	14.5	91.4	0.50	6.9
FR1BH	12.5	805	16.1	6.52, 10.3	14.6	114.9	0.63	4.7
FR2AH	33.0	700	11.8	5.53, 5.99	14.6	99.9	0.55	5.6
FR2BH	33.0	738	12.0	6.08, 6.08	14.6	105.5	0.58	5.8
FR3AH	54.7	674	11.9	4.90, 5.53	14.8	97.6	0.54	5.4
FR3BH	54.7	719	11.7	5.12, 4.76	14.8	104.2	0.57	5.9
FR4AH	—	—	—	—	—	—	—	—
FR4BH	78.5	606	9.7	4.01, 5.20	15.0	88.7	0.49	6.1
FR5AH	99.8	626	12.4	5.26, 5.96	14.7	90.2	0.50	4.8
FR5BH	99.8	657	11.1	4.98, 5.65	14.7	94.7	0.52	5.7
FR6AH	132.5	594	10.8	4.70, 4.61	15.1	87.8	0.48	5.4
FR6BH	132.5	651	12.5	4.58, 4.87	15.1	96.2	0.53	5.1
FR7AH	153.8	594	12.8	4.63, 5.17	15.0	87.3	0.48	4.5
FR7BH	153.8	540	10.9	4.28, 4.53	15.0	79.3	0.44	4.8

from 6 mm near the ice surface, to 17 mm at a depth of 0.7 m, with individual grains becoming difficult to distinguish after 0.7 m due to the strong c-axis alignment. Grain size observations made from the thin sections produced in the present study reveal the same trend and are not significantly different from the previous findings.

Examination of the pole plots obtained from various thin sections through the depth of the ice sheet (see Fig 3.5) made it readily apparent that the ice type was S2, due to the overall horizontal c-axis orientation of the grains. Also visible was the rapid progression of the c-axis alignment towards a dominant azimuth angle of approximately 305 degrees. In Figure 3.5, the first three plots, which were taken from the upper 30 cm of the core, show the rapid initial development of the alignment. Subsequent sections taken at approximately 20

cm intervals through the depth show the continuous increase in alignment, which eventually reaches its peak at approximately 120 cm. As previously mentioned, due to the strong alignment that develops beyond the 0.7 m depth, it was nearly impossible to distinguish individual grains. Therefore, for the remaining thin sections, the pole plots do not so much represent individual grains, but more accurately represent larger bands which are made up of several grains with nearly the exact same c-axis orientation. Although this led to fewer individually plotted points on the graphs, in some cases each point actually represents two or three grains with nearly identical orientations.

After thin sections were made from the crack path region of the specimen, the remaining ice was used for density and salinity measurements. To determine the density, one half of each broken SCB specimen was measured for its radius and thickness with a digital machinist's caliper, and then weighed with a digital scale. The salinity was measured from specimen meltwater using a digital salinity/temperature/conductivity meter. These results, combined with the test temperature, were then used to determine the brine volume and the total porosity by the methods described in Cox and Weeks (1983). Figure 3.5 shows the variation of each parameter with depth in the sheet. Again, comparing the results with those measured by Cole et al (1995) at the time of the field trip shows that the ice primarily maintained its brine content throughout the testing and storage period. It was evident, however, that there was an overall reduction in the salinity by approximately 2 ppt for most of the specimens. This reduction was attributed to sublimation during the prolonged storage period prior to testing and during the testing period when the specimens were warmed to -10°C .

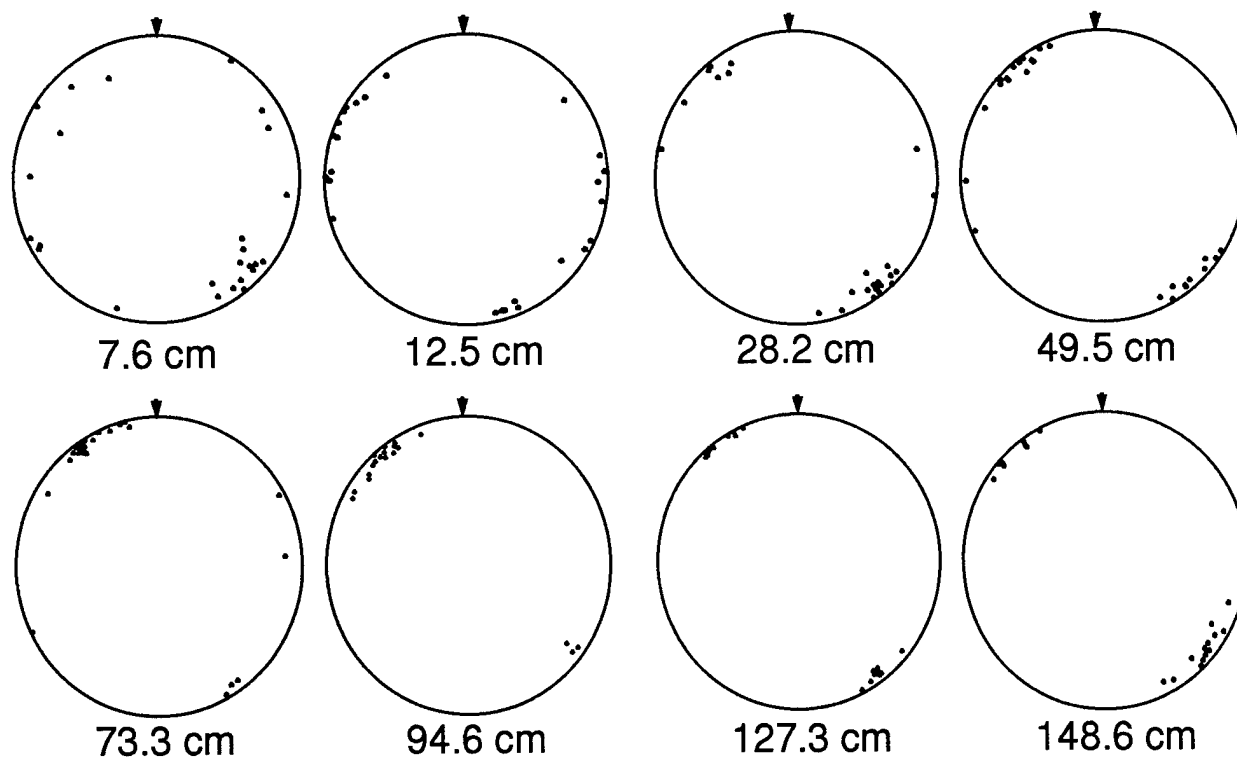
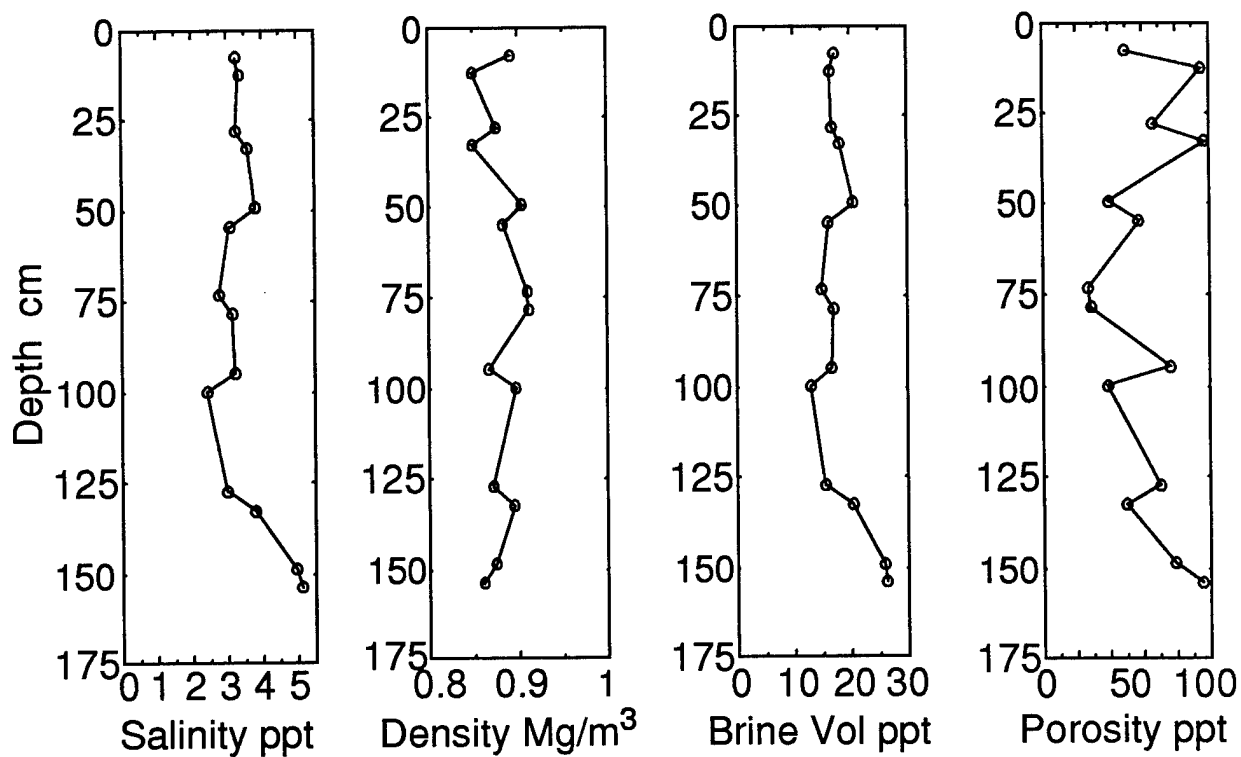


Figure 3.5: Salinity, density, brine volume and porosity vs. depth. Below are Schmidt equal area net pole projections (arrow indicates North or 180°) at various depths through the sheet.

3.7 Influence of C-Axis Alignment

Previous research by Richter-Menge and Jones (1993) on the tensile strength of first year sea ice compares very well with the present test results. In that study, horizontal, columnar first-year sea ice samples were tested in pure uniaxial tension over a range of temperatures and two strain rates. Although measured at a slightly lower strain rate, 75% of the nominal tensile strength values obtained in this study were within one standard deviation of the mean value reported in the previous paper. Both studies indicated a tensile strength of approximately 0.5 MPa at -10°C . Comparison of the elastic modulus determined in each study also showed good correlation, with both finding a range between 4.5 to 7.6 GPa.

Comparing the apparent fracture toughness values obtained in this study with those from previous work has been a difficult task due to a lack of equivalent testing parameters. Because the SCB geometry is relatively new to the ice mechanics community, there have, to date, been no other sea ice fracture toughness studies performed with it. Therefore, comparison must be made with 3pt bending beam tests which were performed on specimens of similar size, and under similar load application rate and temperature range. To date, the only study which has had several key parameters that are similar to this study are the tests performed by DeFranco and Dempsey (1992) on saline ice. In that study, specimen size, \dot{K} , grain size, temperature and crack orientation are all approximately similar to the same parameters in the present work. Results from both studies indicate that the appropriate fracture toughness range is between 80 - 115 $\text{kPa}\sqrt{\text{m}}$, under the testing conditions stated previously.

Unfortunately, a definitive evaluation of the alignment effect, from a quantitative standpoint, is difficult due to variation between the geometry, loading and environmental conditions in these tests and those previously reported by others. However, from a qualitative standpoint there are two significant criteria which indicate that a strong c-axis alignment does cause a measurable decrease in the fracture toughness. First is the issue of grain size. In Urabe and Yoshitake (1981a & b) it is observed that the fracture toughness increases with increasing grain size. This trend was also observed by Timco and Frederking (1982). From the results of the present study, however, the opposite trend is observed. With the increase in depth, and hence increase in grain size, there is a marked decrease in fracture toughness, on the order of 20%.

There are two possible explanations of this observation: (1) the increase in salinity with depth, and (2), the increase in c-axis alignment. Several researchers have observed a decrease in fracture toughness with increasing salinity or brine volume. Post-test analysis of specimens in this study, however, revealed that the salinity remains relatively constant through the depth. Hence, the salinity effect is diminished, and the alignment effect remains as the most likely source of the decrease in fracture toughness. Another indication that the c-axis alignment makes an important contribution is the stabilization of the fracture toughness at a depth of 50 - 70 cm (see Fig 3.4). This corresponds well with the depth at which the alignment has reached a semi-steady state (see Fig 3.5) and stays primarily constant through the remainder of the depth.

Although the test results in Figure 3.4 show a moderate decrease in fracture toughness

and modulus with depth, the trend can not be considered a significant alignment effect. This finding is in direct opposition to the observed behavior of the same ice *in-situ*. During the field testing program, it was quickly determined that the sheet could not be fractured perpendicular to the basal plane without making specific geometry adjustments to account for the substantially higher toughness in this direction. Indeed, the alignment was so strong that the basal plane orientation could be determined *visually* from the direction of tidal cracks present at the ice surface. Therefore, as a secondary evaluation of the laboratory experiments, a psuedo-fracture energy calculation was made from easy and hard fail direction test data. It was initially anticipated that there would be a more significant difference in the energy of fracture, thus making it possible to observe and quantify the alignment effect.

A work-of-fracture estimate of the fracture requires the load-line displacement (LLD), which was not measured. However, a psuedo-work-of-fracture was calculated using the crack-mouth-opening-displacement (δ_{CMOD}) measurements. Although they are not the same quantity, the actual work-of-fracture and the psuedo-fracture energy calculated from the δ_{CMOD} are related by a constant factor. Therefore, although it is not a rigorously obtained quantity, the psuedo-fracture energy is assumed to be adequate for comparison purposes in this study.

Using the high speed load and displacement data (24 kHz) obtained during tests FR1AE and FR1AH, load vs δ_{CMOD} plots for the loading and unloading portions of the experiment were created (see Fig 3.3). The psuedo-fracture energy was then obtained by dividing the area under the load vs δ_{CMOD} curve by twice the area of the uncracked ligament. For both specimens, the psuedo-fracture energy was determined to be approximately 3 J/m². Since

there was no significant difference in energy between the two specimens, this simplified energy approach was considered inconclusive for evaluating the alignment effect. In future work, the authors intend to use a fictitious crack cohesive zone model currently in development (Muhle et al, 1995) to more thoroughly explore the fracture energy aspect of this testing.

3.8 Conclusion

The experimental data presented in this paper are the result of 26 laboratory-scale fracture experiments utilizing the SCB fracture geometry. The tests were performed on specimens cut at regimented depths from a single, full depth, first year sea ice core harvested from Elson Lagoon at Pt. Barrow, Alaska. To correlate the lab tests with field-scale experiments performed during Phase VI of the SIMI project, the cores were collected from the same locations used in the latter tests. All tests were performed at -10°C , which corresponds with the surface temperature present at the time of the field experiments.

The two primary variables between specimens were the orientation of the failure plane with respect to the basal plane and the degree of crystalline c-axis alignment. Of primary interest was the effect of both variables on the apparent fracture toughness, the modulus of elasticity and the tensile strength. Using the expressions for K_{SCB} , E' and σ_{SCB} given in Adamson et al (1996), and the failure load and crack-mouth-opening-displacement of each specimen, each of these quantities was evaluated and then plotted versus depth. K_Q varied between approximately 80 to 115 $\text{kPa}\sqrt{\text{m}}$ with averages of 90.4 and 95.2 $\text{kPa}\sqrt{\text{m}}$ for the easy and hard fail directions, respectively. E' varied between approximately 4.5 to 7.6 GPa with averages of 5.65 and 5.91 GPa for the easy and hard fail directions, respectively.

The nominal tensile strength, as derived from an equilibrium analysis of the SCB geometry, ranged from 0.41 to 0.63 MPa with averages of 0.50 and 0.52 MPa for the easy and hard fail directions, respectively. Each of these quantities compare favorably with previous work by other researchers.

Post-test thin sections were taken from specimens through the depth of the sheet. Using a Rigsby stage, the c-axis orientations of a representative cross-section of grains in each specimen were determined and then plotted on Schmidt equal area nets. The plots indicate the rapid development of a strong horizontal c-axis alignment within the first 30 cm of the core, with individual grains becoming difficult to distinguish because of the extreme alignment beyond 70 cm in depth. Also plotted versus depth were the post-test salinity, density, brine volume and porosity. All of the fabric and bulk property measurements on the ice were found to be in good agreement with the more detailed measurements taken during the field testing program (Cole et al, 1995).

The work-of-fracture was estimated for specimens in the easy and hard fail directions to further investigate the unexpectedly small difference in fracture toughness between them. A psuedo-fracture energy calculation was made based on the crack-mouth-opening-displacement, rather than the load-line displacement. Using a high-speed (24kHz) data acquisition system, the unloading portion of the curve was captured, thus allowing calculation of the psuedo-fracture energy from the complete load vs δ_{CMOD} plot. Based on this calculation, there was again no significant difference found between the easy and hard fail specimens.

The lack of a significant difference between the easy/hard fail specimens is surprising

when compared with the observations made in the field testing program. During the in-situ program it was found to be impossible to propagate fracture in the hard fail direction without substantially modifying the test geometry. For this reason, it would be ideal to repeat this testing program on sea ice which lacks a strong c-axis alignment so that its effect can be isolated. This would not only create a better information base for this geometry under these laboratory environmental conditions, but would also have implications for the issue of scale in the alignment effect.

4 A BROAD-SPECTRUM CONSTITUTIVE MODEL FOR SALINE ICE³

4.1 Abstract

The constitutive behavior of lab-grown saline ice subjected to isothermal, uniaxial tensile loadings is discussed. A rectangular plate specimen of S2 columnar saline ice was subjected to a uniform tensile stress perpendicular to the long axis of the column structure. This loading was selected to represent the stress field which occurs in the plane of natural ice covers under tension. The uniaxial stress state was applied with the recently developed, modified Reversed Direct Stress device detailed in LeClair et al (1996). Two successive load histories were applied – creep-recovery cycles and monotonic stress ramps. A broad-spectrum, nonlinear viscoelastic modeling approach developed in Schapery (1969) for polymer research is used to develop a constitutive model of the strain response. Each parameter of the model is evaluated from the measured ice response to the creep-recovery loadings. The model provides an accurate representation of the experimental data with a delayed elastic compliance function in time power law form (t^n , $n = 1/3$) and a nonlinear stress exponent (σ^q , $q = 3/2$). Finally, the model is used to predict the strain response of the ice to the monotonic ramp loadings with good results.

4.2 Introduction

Over the past several years, the authors have been conducting research as part of the Accelerated Sea Ice Mechanics Research Initiative (SIMI) project sponsored by the Office of

³To be submitted to the *International Journal of Fracture*, September 1996.

Naval Research. One of the primary objectives of the SIMI project has been to develop an accurate constitutive model that describes the behavior of sea ice when it is subjected to various types of loading. In this study, the strain response of laboratory-grown saline ice to pure tension creep-recovery and monotonic ramp loadings was examined. Specifically, S2 transversely isotropic ice specimens were loaded normal to the columnar grain structure by uniform uniaxial tensile stress under isothermal conditions.

This paper contains the details of an experimental program which was planned from existing nonlinear viscoelastic constitutive theory to both evaluate the parameters of, and verify a rigorous constitutive model for sea ice. Firstly, a full description of the experiment is provided. Included are details of the specimen growth and preparation, strain measurement, data acquisition and post-test analysis. Also included is a brief description of the unique tensile loading device (Cole and Gould, 1989,1990; LeClair et al, 1996) used to apply stress to the rectangular plate ice specimen.

Secondly, a basic derivation of the theoretical model for the specific conditions of the laboratory experiment is provided. The theory originates from an article by Schapery (1969), wherein a procedure is outlined by which the characteristic constitutive equation of a nonlinear viscoelastic material may be determined from experimental constitutive data obtained in a single creep-recovery loading experiment. For brevity, only the derivation of the elastic, viscous and delayed elastic components of the total strain response to uniaxial loading under isothermal conditions is presented here. The full derivation of the constitutive equation from general, multi-axial nonlinear viscoelastic theory is available, however, in the original article.

Finally, the investigative process for determining each parameter of the model is described. By taking advantage of observations made from the experimental creep-recovery data, several simplifications are made in the governing constitutive equation. Using convolution integrals, the individual strain components are then determined numerically and combined using superposition to obtain a model of the total strain response. To test the final model's versatility, it is also used to predict the strain response of the ice used in the creep-recovery experiment to a series of monotonic ramp loadings.

4.3 Creep-Recovery Experiment Details and Results

The ice specimen used in this experiment was cut from a sheet of columnar S2 saline ice grown in a $1.2 \times 1.2 \times 1.2$ m basin at Clarkson University. To develop this ice type, a 26 ppt concentration saline solution was chilled to approximately -1°C and then seeded by spraying a fine mist of the solution into the frigid air above the liquid surface. As the mist cooled in the frigid air above the tank it formed small ice crystals, which then settled on the liquid surface. Gradually, a thin, but visible layer of seed ice formed over the entire surface. To further aid development of a vertical columnar structure in the ice, the growth basin was equipped with pressure relief valves near its base. This feature provided an outlet for the remaining liquid solution at the bottom of the basin as the volume of the growing ice sheet increased.

After one week the seed layer had developed into a sheet with a depth of approximately 30 - 35 cm. At this time the sheet was cut into several large blocks, which were removed from the basin and stored at -23°C . The test specimen was later cut from near the bottom

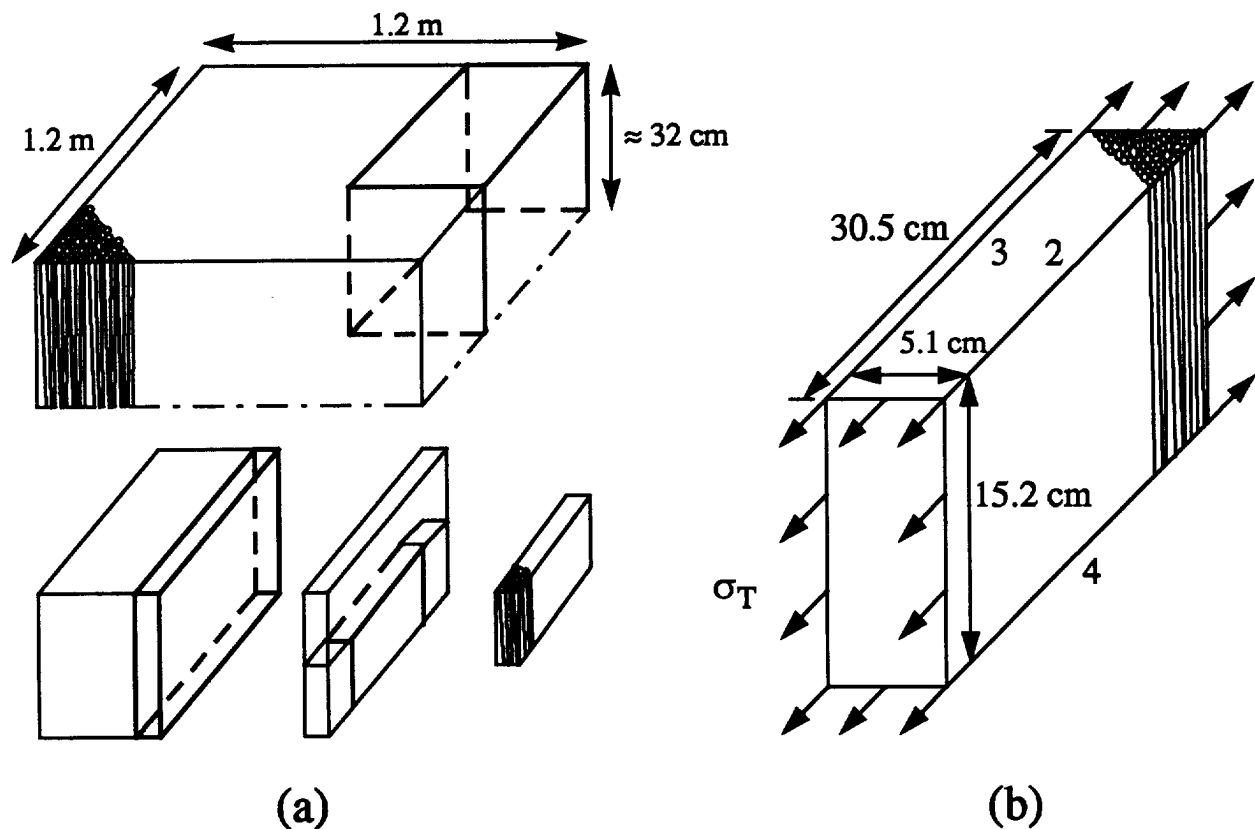


Figure 4.1: (a) Location of specimen T302 in the original ice sheet, (b) Stress was applied to the ice along the length of the columns, producing a stress field similar to in-situ, in-plane tensile forces.

of a block and machined to size (see Fig. 4.1a). The cross-sectional dimensions (15.2 cm \times 5.1 cm) were dictated by the end cap dimensions of the testing device. A 2:1 length-to-width ratio ($L = 30.5$ cm) was provided to limit end effects on the strain measurements.

During preparation, the specimen was cut from the block such that failure would occur in a plane perpendicular to the surface of the ice sheet as shown in Fig. 4.1. This produced the effect of subjecting the specimen to in-plane tensile forces similar to those present in-situ. The specimen was then wrapped in plastic to reduce sublimation and stored at -27°C . Prior to testing, the specimen was fitted with end caps according to the methods described in LeClair et al (1996). The end caps were necessary to incorporate the specimen into the

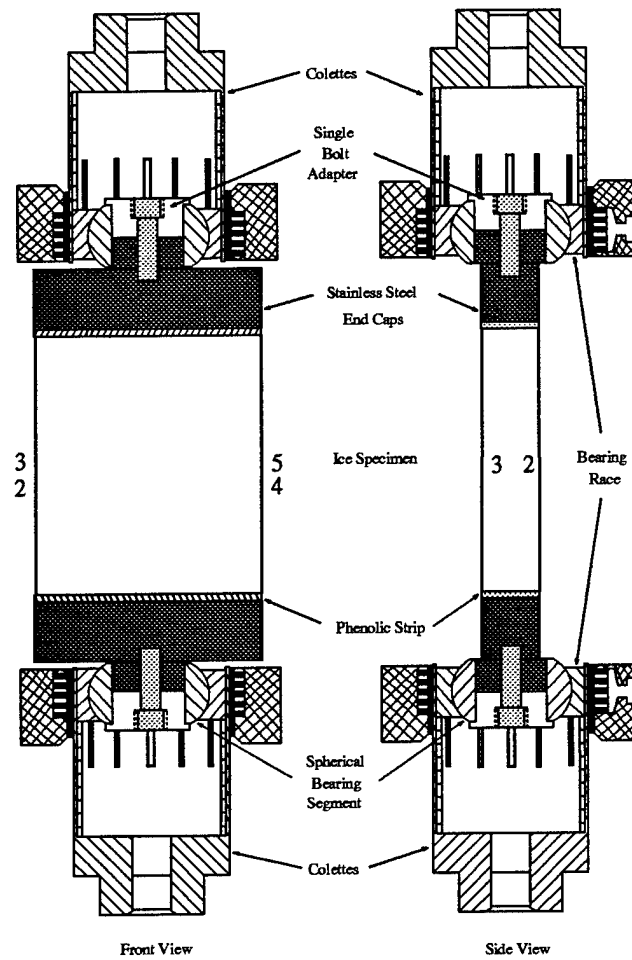


Figure 4.2: The modified Reversed Direct Stress (RDS) device.

special tensile loading device described later. Finally, the endcapped specimen was moved to the testing cold chamber, where it was allowed to acclimatize overnight prior to the isothermal, -15°C experiment. The entire process, from growth, to storage and finally to testing, took place over a period of 4 months.

On the test date, four LVDT gages were attached at various points on the specimen and the end caps. With the use of specially designed aluminum cantilever supports (see Fig. 4.3), the gage length was extended to measure displacement over both the central 80% and the

total specimen length. The latter was achieved by bolting the support directly to the steel end cap. During the analysis, the strain in the steel and phenolic portions of the end cap was assumed to be negligible, thus equating the second gage length with the full length of the specimen (30.5 cm). All of the gages were mounted on the 5.1 cm faces so that displacement was measured at the extremes of the columnar growth in the ice. On each of these faces, one cantilever gage was bolted directly to the ice and the second was bolted to the end cap. With the gages in place, their corresponding targets were attached with the same methods and locations.

The uniaxial tensile stress necessary for this experiment was applied with the modified version of Cole's Reversed Direct Stress device (Cole and Gould, 1989 & 1990) detailed in LeClair et al (1996) (see Fig. 4.2). The RDS device was designed to alleviate two common problems in tensile ice testing. First, it adapts to the non-parallel end planes of an ice specimen, thus allowing it to attach the specimen to a properly aligned test frame. Second, it prevents any shift in the loading axis (a common problem with universal joints) due to deformations in the specimen. These features allow the RDS to apply a constant, uniaxial stress field to an ice specimen, despite any end plane misalignment (LeClair et al, 1996).

After the gages were securely attached, the entire assembly was mounted in the load train. Once seated in the colettes, the bearing race on each end cap was clamped in place with the hydraulic clamps of the RDS device. The closed loop, servo-hydraulic actuator was then transferred immediately to load control with the load set at 10 N. This small tensile load (compared to the creep stress levels) was required at all times for the actuator to maintain

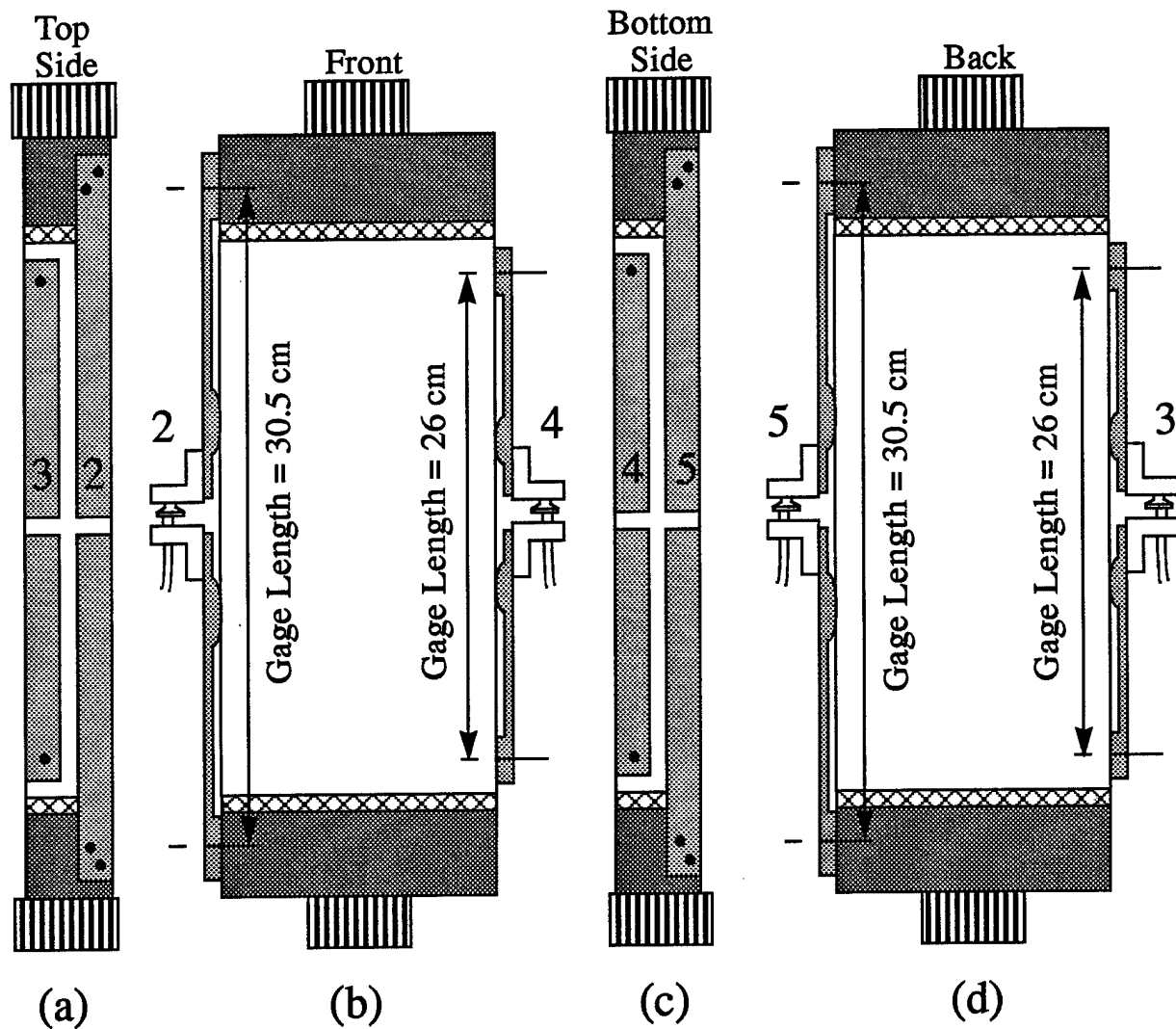


Figure 4.3: Strain response was measured with cantilevered gage mounts over both the central 80%, and the full length of the specimen. Parts (a) and (c) show the gage positioning on the left and right sides (from the front view (b)), respectively.

control of the specimen in tension.

The creep-recovery loading sequence consists of an arbitrary number of constant stress applications, separated by zero stress recovery periods. In this experiment, each sequence was composed of three alternating stress/hold, release/recovery periods. Over the duration of the test, three full sequences totaling nine individual constant stress applications were applied at stress levels of 0.13, 0.23 and 0.32 MPa (see Fig. 4.4). Through the computer

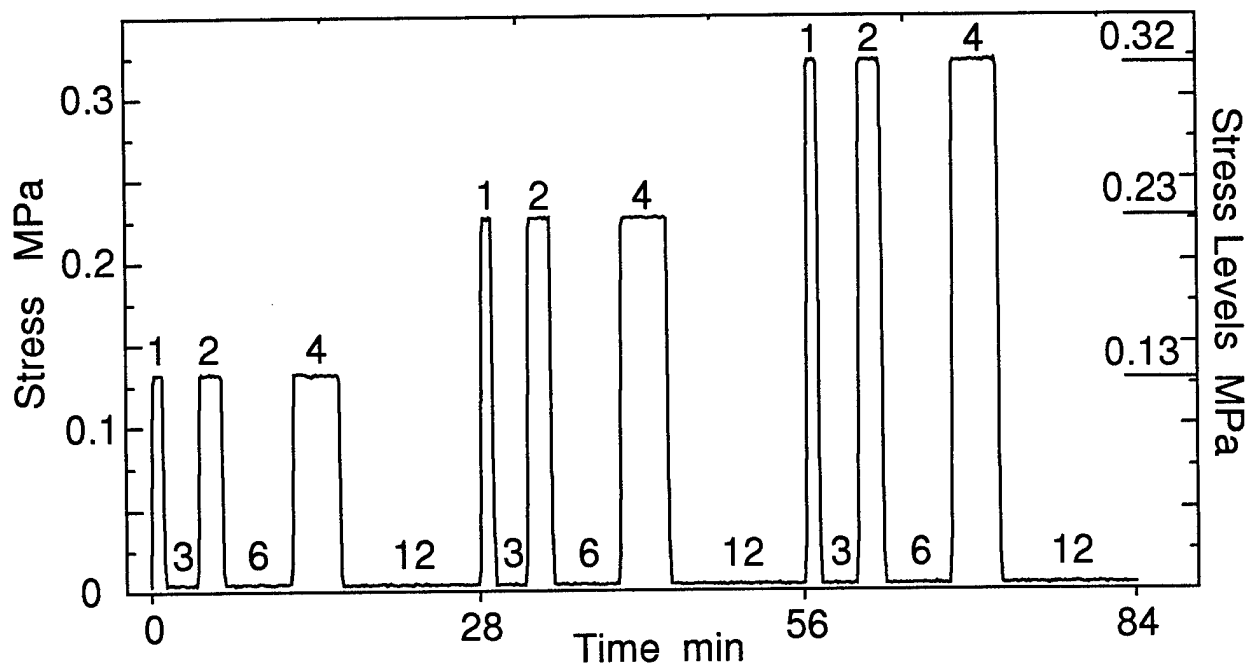


Figure 4.4: Stress vs time as recorded during experiment T302. The number on each segment indicates the duration of each creep and recovery period (in minutes).

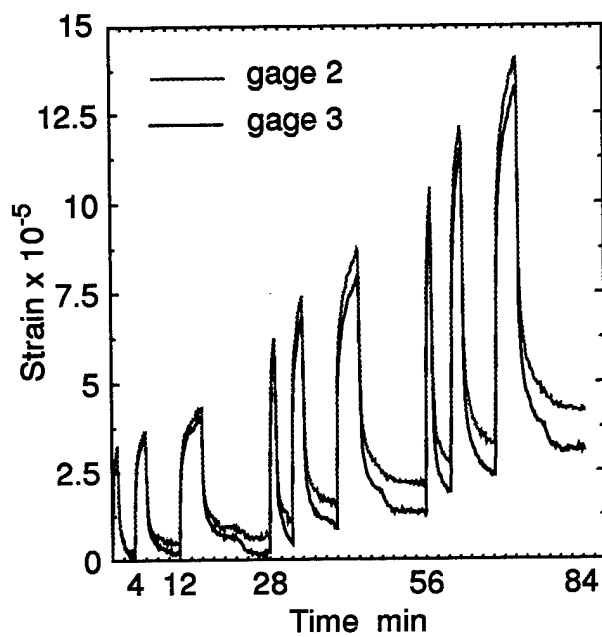
controlled actuator, each stress was applied as a trapezoidal wave function. The slope of the wave on load-up was 500 N/s for the 0.13 and 0.23 MPa stress levels, and 1000 N/s for the 0.32 MPa stress level. The wave slope on load-release was 1000 N/s for the 0.13 and 0.23 MPa stress levels, and 1750 N/s for the 0.32 MPa stress level. While the trapezoidal wave did not produce an instantaneous stress application, in each case the stress was applied in 2.5 seconds or less and released in 2 seconds or less. These rates were chosen based on previous experience to avoid premature failure of the specimen.

Once at the desired level, the stress was held constant for a predetermined time interval. In this experiment, each interval was a multiple of the basic time step, $\Delta t = 1$ minute. For each successive creep stress period, the multiple of the time interval was doubled, e.g. 1, 2, 4. As previously mentioned, the creep stress periods were separated by the zero stress recovery

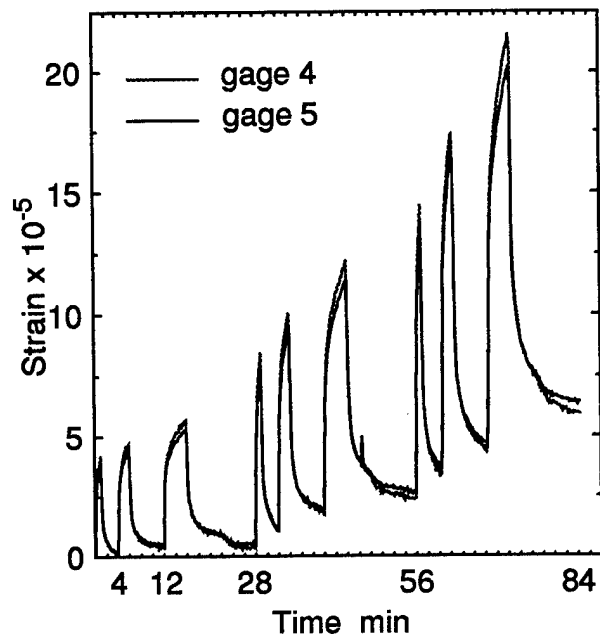
periods. The recovery time intervals were also functions of the basic time step, Δt , with the minimum interval starting at $3\Delta t$, and, as with the creep stress periods, successively doubled, e.g. 3, 6, 12. When the first creep-recovery sequence (0.13 MPa) was complete, the same time interval pattern was repeated for the second and third sequences. The full stress history as recorded during the experiment is illustrated in Fig. 4.4.

Using the previously discussed extended gage lengths, the displacements measured by the LVDT gages were transformed to strains. The resulting strain response of the ice is shown in Figs. 4.5a - d. When closely examined, the strain records revealed that although the gages mounted on the same specimen face were very similar (see Figs. 4.5a & 4.5b), there was a measurable difference between the opposing sides. Fig. 4.5c compares the averaged strain response from each side of the specimen (2,3 ; 4,5) with the difference between the them, $\Delta\epsilon$. This difference was apparently due to rotation of the RDS device caused by the varied microstructure and morphology that formed during the growth of the ice sheet. Note in Fig. 4.1 that gages 2 and 3 were attached to the 'top' side, while gages 4 and 5 were attached to the 'bottom' side of the specimen, 15.2 cm lower down in the columnar growth structure.

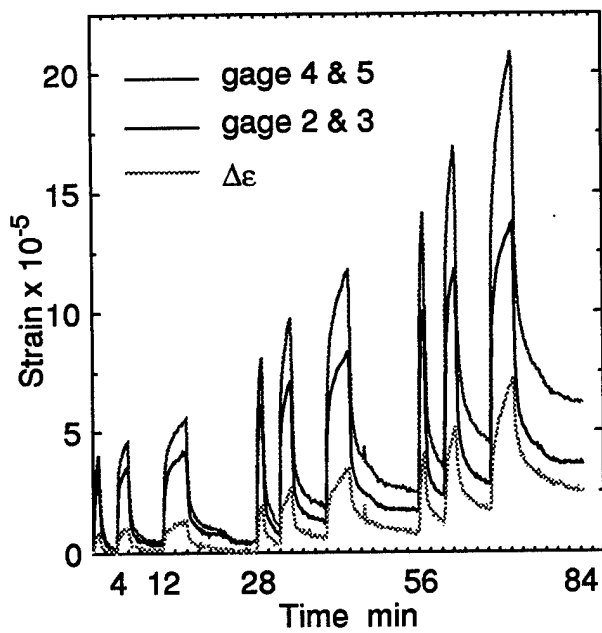
While this difference was attributed to rotation of the device, the actual amount of rotation is minimal. If one end cap is assumed to rotate about the midpoint between the gages and \pm one half of the strain difference $\Delta\epsilon$ is assigned to each of the two faces, the actual rotation of the device was determined as approximately 7.5 thousandths of one degree. In fact, if the strains had not been measured with such accurate LVDT gages, it is unlikely that any rotation could have been observed at all. Ultimately, the average of the four strain



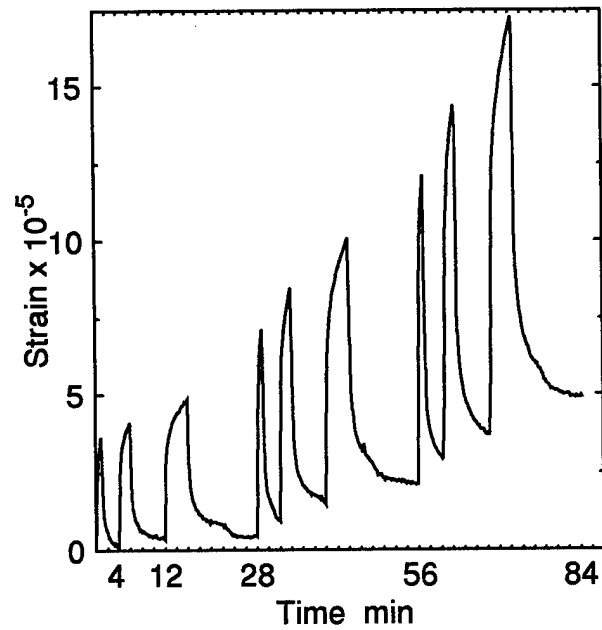
(a)



(b)



(c)



(d)

Figure 4.5: Strain vs time data obtained from the LVDT gages. Graphs (a) & (b) show the similarities between gages mounted on the same specimen face, (c) depicts the difference in strain between the opposing faces and (d) is the four gage average used for numerical modeling.

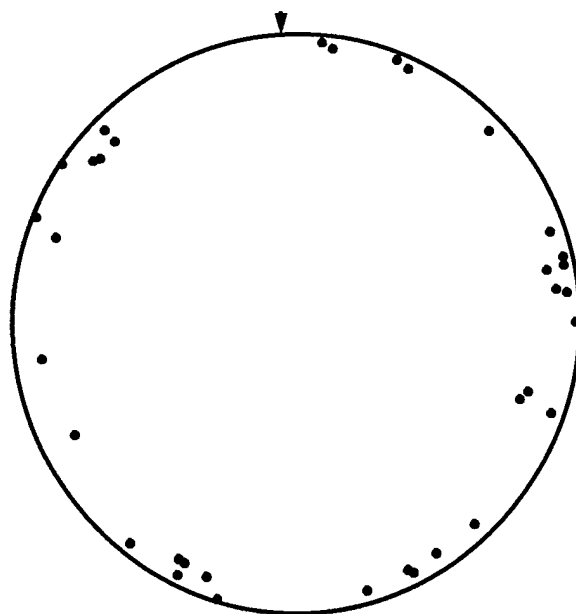


Figure 4.6: Schmidt equal area net pole projection for the saline ice used in experiment T302.

records (see Fig. 4.5d) was used as the basis for the ensuing numerical model to reflect the bulk strain behavior of the ice.

Immediately following the creep-recovery sequences, six tensile monotonic stress ramps were applied to the specimen. In each test, the stress was ramped linearly from approximately 0 to 0.26 MPa, over several rates. The times to reach peak load for each test were 2, 20, 200, 400, 2000 and 2 seconds, respectively. Unloading occurred in 1 second for both 2 second tests and the 20 second test, and in 2 seconds for the remaining tests. At the end of each unloading, the specimen was allowed to recover any induced strains until no change in the gage output was noticeable. The strain response was again recorded with the four LVDT gages, positioned in the same manner as the previous experiment. As with the creep-recovery loadings, each monotonic test was performed isothermally at -15°C . The strain response due to each ramp is depicted in Figs. 4.10 and 4.11 along with the corresponding modeled strain

response. Also shown is the contribution of each individual strain component to the total strain response.

With the testing complete, a post-test microstructural analysis was performed. Using a Rigsby stage (Langway, 1958), thin-sections from the top and bottom of the specimen's column structure were examined to determine the grain size and create a c-axis projection plot (see Fig. 4.6). The grain size was found to be approximately 10 mm and the horizontal grouping of pole projections on the plot confirmed that the specimen was composed of randomly oriented S2 ice. Further analysis of the remaining ice according to the techniques in Cox and Weeks (1983) revealed the salinity (6.5 ppt), density (0.897 Mg/m^3), brine volume (10.1 ppt) and porosity (52.4 ppt).

4.4 Uniaxial, Isothermal Constitutive Equation

As previously mentioned, only the nonlinear viscoelastic equations for axial strain ϵ due to constant, uniaxial creep stress σ under isothermal conditions ($\Delta T = 0$) are presented here. The complete development of the general form of these equations from a multiaxial nonlinear theory is presented in Schapery (1969 & 1996). The equations were first developed from nonlinear thermodynamics using the concept that any linear material may be modeled by a series of springs and dashpots. From this concept, the axial strain (ϵ) has been shown to equal the sum of the elastic ϵ_e , viscous ϵ_v and delayed elastic ϵ_d strain components,

$$\epsilon = \epsilon_e + \epsilon_v + \epsilon_d \quad (5)$$

where

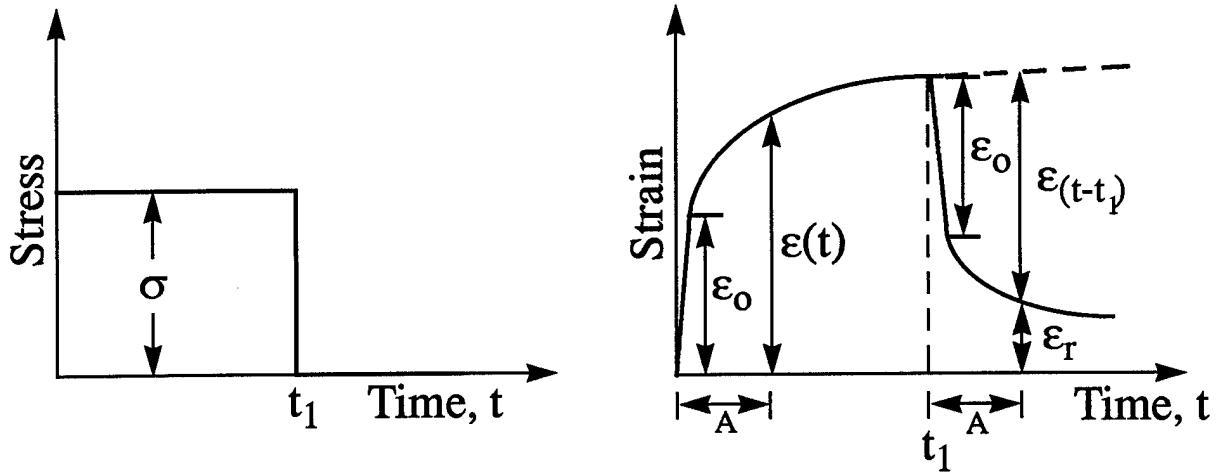


Figure 4.7: An idealized representation of the creep and recovery of a linear viscoelastic material. (After Schapery, 1969)

$$\epsilon_e = g_o S_e \sigma \quad (6)$$

$$\epsilon_v = S_v \int_{-\infty}^t g_v \sigma dt' \quad (7)$$

$$\epsilon_d = g_1 \int_{-\infty}^t S_d (\psi - \psi') \frac{dg_2 \sigma}{dt'} dt' \quad (8)$$

and

$$\psi - \psi' = \int_{t'}^t dt'' / a_\sigma [\sigma(t'')] \quad (9)$$

In the above equations, g_o , g_v , g_1 , g_2 and a_σ are typically functions of stress, the coefficients, S_e , S_v and S_d , are the elastic, viscous and delayed elastic compliances, respectively, and σ is the applied stress. Note that due to the isothermal condition ($\Delta T = 0$), there is no temperature effect included in these simplified equations.

As outlined in Schapery (1969), each of the functions in the above equations may be fully determined by subjecting a material to one cycle of a creep-recovery test. The creep loading portion of this test may be represented (neglecting, for the moment, the non-zero, but very small time durations to load up and unload)

$$\sigma = [H(t) - H(t - t_1)] \sigma_o \quad (10)$$

where H is the Heaviside unit step function, $H(t - t_1) = 1$ for $t > t_1$, and $H(t - t_1) = 0$ when $t < t_1$, and σ_o is the constant creep stress. To simplify the notation, two new stress functions,

$$f_1 \equiv S_v g_v \sigma \quad , \quad f_2 \equiv g_2 \sigma \quad (11)$$

are introduced. Combining (11) with (10), for one cycle of a creep-recovery test with stress σ_o and $i = 1, 2$,

$$f_i = [H(t) - H(t - t_1)] f_{io} \quad (12)$$

Then, substituting the creep stress and the functions f_i into (5), the expression for the strain component due to creep loading is found to be

$$\epsilon = S_e \sigma + f_1 t + f_2 S_d(t) \quad , \quad 0 < t < t_1 \quad (13)$$

Similarly, noting that σ_o is zero during the recovery period and again substituting f_i in (5), the strain component due the zero stress recovery 'loading' is described by

$$\epsilon_r = f_1 t_1 + f_2 [S_d(t) - S_d(t - t_1)] \quad , \quad t > t_1 \quad (14)$$

Note that for the recovery strain,

$$\epsilon_r = \epsilon(t) - \epsilon(t - t_1) \quad (15)$$

The result in (15) shows that, for all times $A > 0$, the strain due to creep equals the difference between the recovery strain and the predicted creep strain if loading were to continue (see Fig. 4.7). While this is true in general for linear viscoelastic behavior, it is only true for the special case of $g_1 = a_\sigma = 1$ for nonlinear viscoelastic behavior. Also evident from (15) is the ability to determine the recovery strain from the superposition of two creep strains, which is valid for the particular nonlinear behavior implicit in (5) - (8). This is a direct result of the condition that $g_1 = a_\sigma = 1$, and is the basis of the numerical modeling of the strain history discussed in the next section.

4.5 Numerical Modeling of S2 Saline Ice Strain Response

Using the nonlinear viscoelastic theory outlined in the preceding section and the results of the previously described creep/recovery experiment, a numerical model can now be developed for predicting the strain response of saline ice specimens to any arbitrary loading. The basis of the following numerical analysis lies in the ability to use the superposition of creep strains to determine the recovery strain. For the nonlinear viscoelastic behavior described in (5) - (8), this is only possible for the case when $g_1 = a_\sigma = 1$. Hence, the first step of the analysis is to show that the experimental data exhibits this characteristic.

The rigorous analytical methods for determining the stress functions g_1 and a_σ are thoroughly discussed in Schapery (1969). However, by taking advantage of two key characteristics of the experimental data, their determination is greatly simplified. Referring to Figure 4.7, it can be seen that for a linear viscoelastic material, the initial elastic jump in strain ϵ_o at $t = 0$ is equal to the instantaneous drop in strain at $t = t_1$. For a nonlinear material, however, this is not necessarily true. It can be shown from (6), (7) and (8) for a two-step loading (e.g. creep-recovery loading) that the difference between the two strain jumps has the form

$$\Delta\epsilon_o = g_2(g_1 - 1)S_d(t_a/a_\sigma)\sigma \quad (16)$$

If it is found that $\Delta\epsilon_o \approx 0$ for the nonlinear experimental data, then $g_1 = 1$. Examination of the present experimental data revealed that this was true.

Referring now to a general representation of the nonlinear strain due to a single arbitrary creep-recovery cycle (Fig. 4.8a) and the result of (15), for all $0 < A < t_1$, the strain due to creep equals the difference between the recovery strain and the predicted creep strain if loading were to continue. If this relation is shown to be true for nonlinear creep-recovery data over the full range of time and stress used in the experiment, Equations (6), (7) and (8) for a two-step loading show that $a_\sigma = g_1 = 1$. To show that this condition applies for the current data, the first and third creep and subsequent recovery periods at the highest stress level were numerically modeled and then shifted such that they both initiated at the same arbitrary reference time. The model strain response of the longer third creep period was then assumed to represent the predicted strain due to creep loading if the first creep

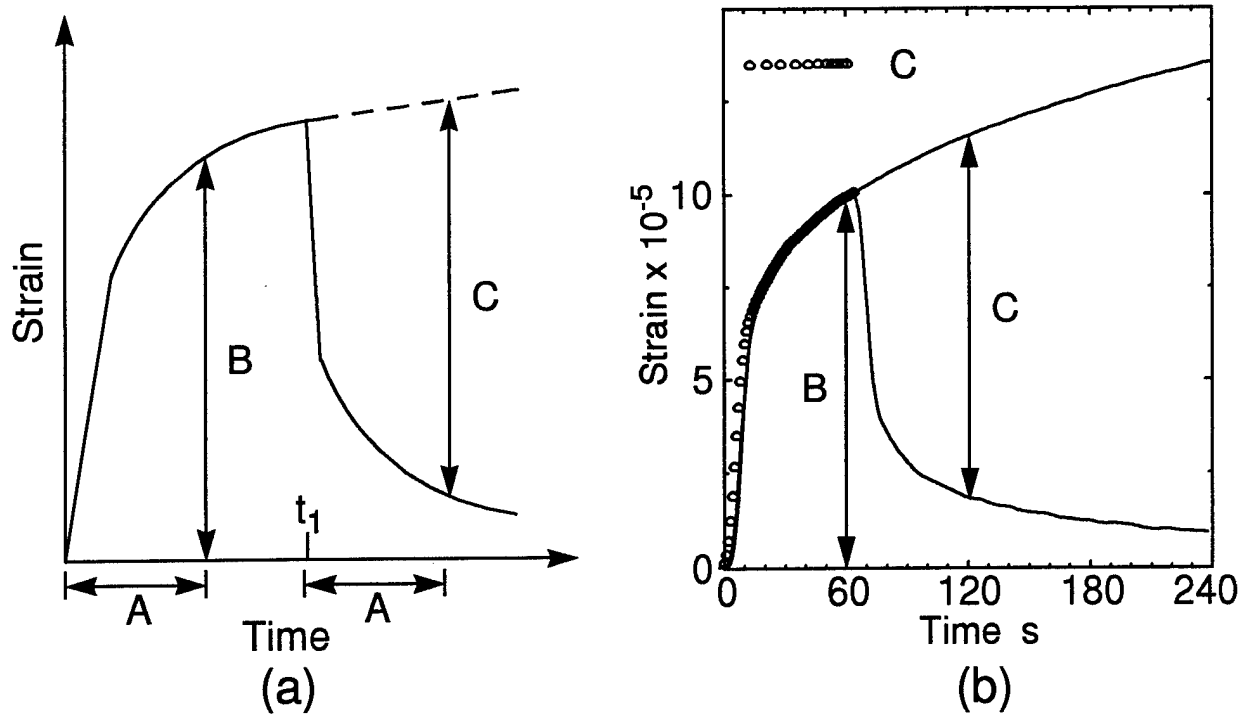


Figure 4.8: (a) Idealized representation of a nonlinear creep-recovery strain history. (b) Data from this creep-recovery experiment shows that from (a), $B = C$, and therefore the stress functions $g_1 = a_\sigma = 1$.

loading had been held for a longer duration. By subtracting the recovery strain associated with the first creep loading from the creep strain of the third loading, the quantity ϵ_{t-t_1} was determined. Figure 4.8(b) shows the modeled creep data with ϵ_{t-t_1} shifted to the reference time and plotted over the creep strain due to the first loading. As can be seen, $\epsilon(t) = \epsilon_{t-t_1}$ over the entire duration of the first creep stress application, thus showing graphically that $a_\sigma = g_1 = 1$ for the experimental data.

The form of the stress function g_0 is designated by the material's elastic constitutive behavior. Most materials exhibit linear strain behavior within the elastic stress range, hence yielding $g_0 = 1$. This characteristic is often observed with ice and it will also be assumed to apply for the specific ice type used in this experiment. Therefore, the stress function $g_0 = 1$.

The remaining stress functions g_v and g_2 , along with the compliance constants S_e and S_v , and the time function $S_d(t)$ were determined numerically with an iterative convolution integral approach. Since the stress dependence of the viscous and delayed elastic strain components were initially unknown, the stress functions f_1 and f_2 were redefined as

$$f_1 = S_1 \sigma^p \quad , \quad f_2 = S_2 \sigma^q \quad (17)$$

to allow nonlinear stresses. Recalling the initial form of f_i in (11),

$$g_v = \sigma^{p-1} \quad , \quad g_2 = S_2 \sigma^{q-1} \quad (18)$$

with $S_v = S_1$ and S_2 introduced as a delayed elastic compliance constant. Due to the short duration of the creep loadings and accuracy at early times, a power law was assumed for the time function, $S_d(t) = t^n$, where typically $0 \leq n \leq 0.5$.

With the aid of DADiSP data analysis software, each component of the strain was evaluated individually using a convolution integral approach. The three strain components were then superposed to obtain the final overall strain response to the three creep-recovery stress sequences. The first task in this process was to evaluate the derivative of the appropriate stress function for each component. In initial attempts, the elastic and delayed elastic components were both modeled using linear stress functions (σ ; σ^q , $q = 1$, respectively), i.e. the derivative of the unmodified creep-recovery stress record. For the viscous strain component, the cubic stress function (σ^p , $p = 3$) commonly used in dislocation theory models was chosen. Next, three data series' representing the compliance functions S_e , $S_1 t$ and $S_2 t^n$ were created.

Each of these compliance function series' had the same frequency and length (# of data points) as the three corresponding stress function derivatives. Finally, the compliance functions were numerically convolved with the corresponding stress function derivatives. This yielded the elastic, delayed elastic and viscous strains as three separate components. The total strain response was then obtained by superposing the three individual strain components.

Repeated attempts to match the experimental data with a model of this initial form were met with limited success. It was observed that the viscous strain component predicted by the model was considerably lower than its counterpart found in the experimental data. However, a closer examination of the experimental strain data showed that the recovery periods were too short to allow for full recovery of the delayed elastic strain accumulated during the creep stress applications. Therefore, the strain component of the experimental data initially thought to be only the viscous strain was actually a combination of the true viscous strain and a gradually increasing portion of the unrecovered delayed elastic strain component. To account for this unrecovered delayed elastic strain in the model, the stress dependence of this strain component was altered to a nonlinear form, i.e. $q > 1$. This allowed the model to develop the necessary unrecovered delayed elastic strains. Subsequent iterations with the stress function derivative yielded a good approximation of the data with $q = 3/2$.

The determination of each model parameter began by modeling specific portions of the creep-recovery data to obtain some initial approximations. The terms S_e , f_2 and $S_d(t)$ were

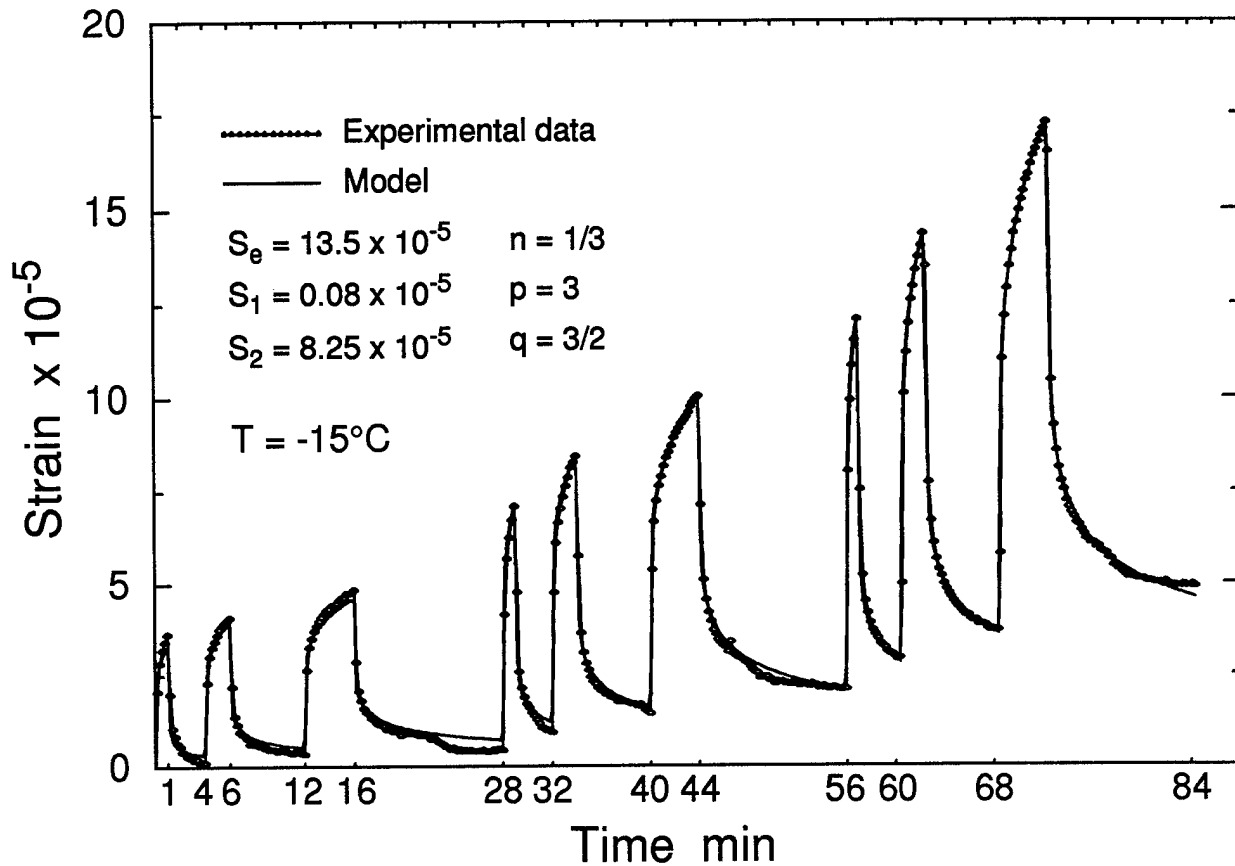


Figure 4.9: (a) Experimental and model strain response obtained with the given model parameters and (b) the individual model strain components.

approximated first from the creep portion of the 1 min creep - 3 min recovery cycle at the two lowest stress levels (0.13 MPa & 0.23 MPa) with the viscous strain component extracted from the data. After several iterations, the values of n , S_e and f_2 were determined by comparing plots the model strain vs t^n to the experimental data until a good approximation was made. From this initial analysis, a value of $n = 1/2.5$ was found to best represent the data. Using this estimate of n and the estimates of S_e and f_2 , the final values of all the model parameters were determined iteratively by comparing the model strains to the experimental strain data over all of the creep-recovery cycles.

After several iterations, a model strain response was determined which provided an excellent fit of the averaged experimental strain data over all three of the creep-recovery sequences. The final model parameters, with σ in units of MPa and t in seconds, are

$$S_e = 13.5 \times 10^{-5} , S_1 = 0.08 \times 10^{-5} , S_2 = 8.25 \times 10^{-5}$$

$$p = 3 , q = 3/2 , n = 1/3 \quad (19)$$

Figure 4.9 shows the model strain response plotted with the average strain vs time from experiment T302. Closer examination of the elastic compliance shows that the model predicts a modulus of elasticity of approximately 7.4 GPa.

Finally, incorporating the above expressions and recalling that $g_o = g_1 = a_\sigma = 1$, the general form of the strain response for S2 saline ice to an arbitrary stress history is

$$\epsilon = S_e \sigma + S_1 \int_{-\infty}^t \sigma^p dt + S_2 \int_{-\infty}^t (t - t')^n \frac{d\sigma^q}{dt'} dt' \quad (20)$$

In the next section, the validity of this general equation is tested by applying it to experimental constitutive data obtained from a series of monotonic stress ramps imposed on the same S2 saline ice specimen.

4.6 Application to Monotonic Stress Ramp Data

Perhaps the most valuable asset of this constitutive modeling technique is that the resulting model can be applied to any arbitrary stress history. To verify that this statement is true for the model outlined by (20), the model was applied to constitutive data obtained from a

series of monotonic stress ramp loadings. The ramps were applied to the same S2 saline ice specimen approximately 30 minutes after completing the final creep-recovery sequence.

After completing the creep-recovery loading sequences, six tensile monotonic stress ramps were applied to the specimen. In each test, the stress was ramped linearly from approximately 0 to 0.26 MPa, over several rates. The times to reach peak load for each test were 2, 20, 200, 400, 2000 and 2 seconds, respectively. Unloading occurred in 1 second for the two 2 second and the 20 second tests, and in 2 seconds for the remaining tests. At the end of each unloading, the specimen was allowed to recover any induced strains until no change in the gage output was noticeable. The strain response was again recorded with the four LVDT gages, positioned in the same manner as the previous experiment. As with the creep-recovery loadings, each monotonic test was performed isothermally at -15°C . The resulting strain response from each monotonic test is depicted in Figs. 4.10 & 4.11 along with the modeled strain response. Also shown is the contribution of each individual strain component to the total strain response.

Comparing the model results with the corresponding experimental data, it is seen that overall the model provides a fairly accurate representation of the actual strain response. In each case, with the exception of the longest time duration ramp (2000 s), the model is most accurate during the loading portion of the ramp. It was also successful in predicting the peak strain values for all load durations. In general, the model best predicts the strain response in tests where loading was held for approximately the same time duration as the creep-recovery sequences.

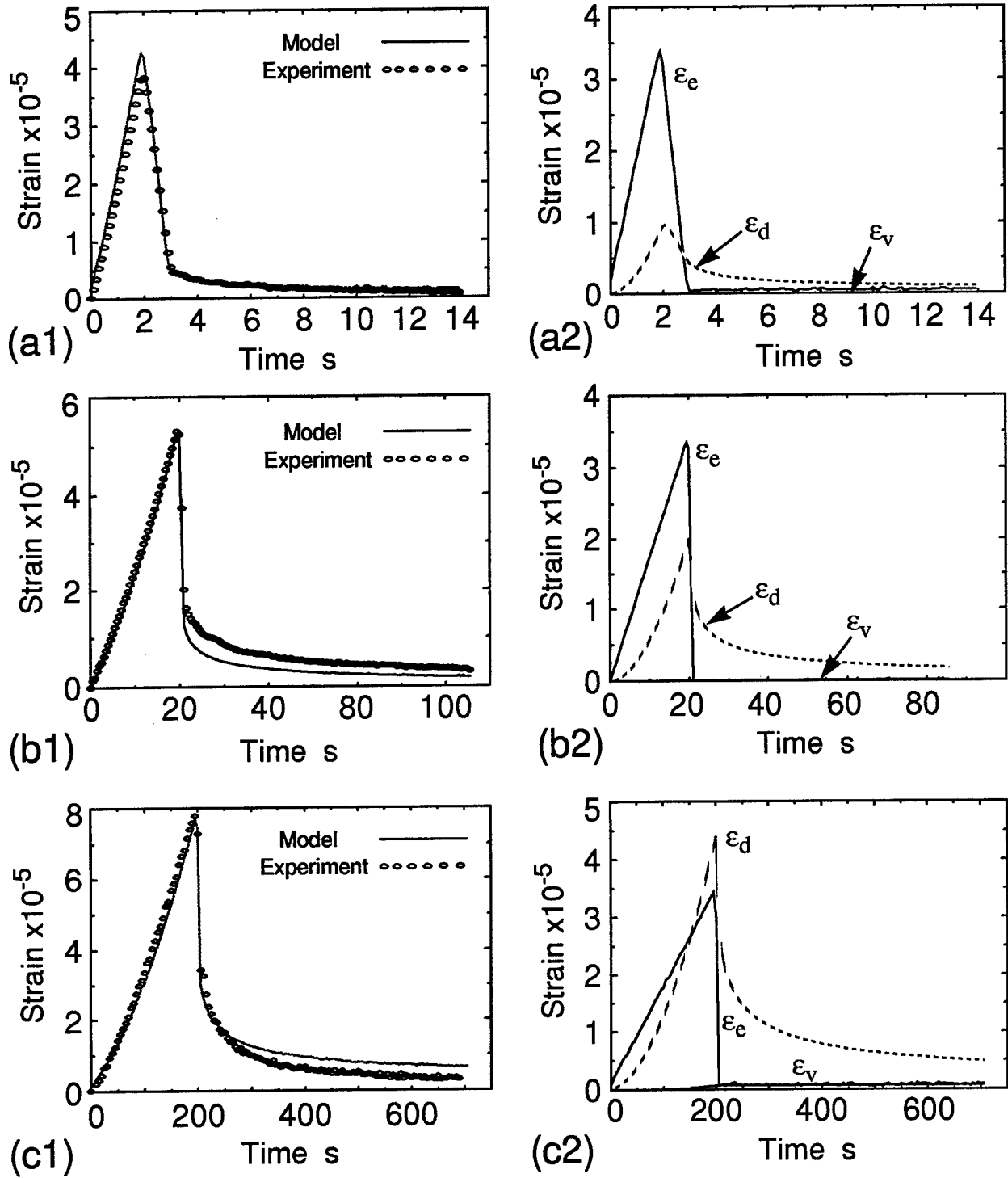


Figure 4.10: (a1) - (c1) Experimental and model strain response to monotonic stress ramps and (a2) - (c2) the individual strain components of each model.

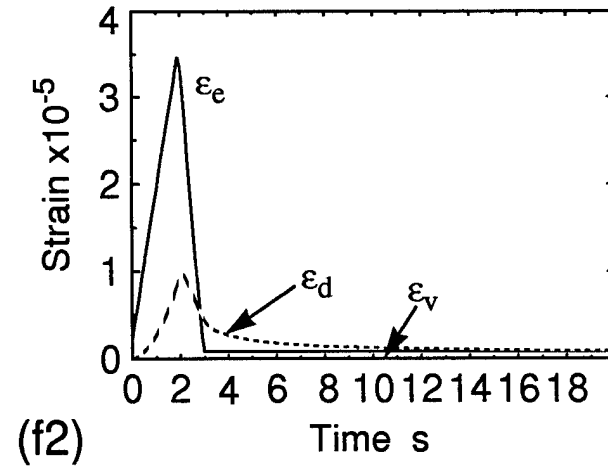
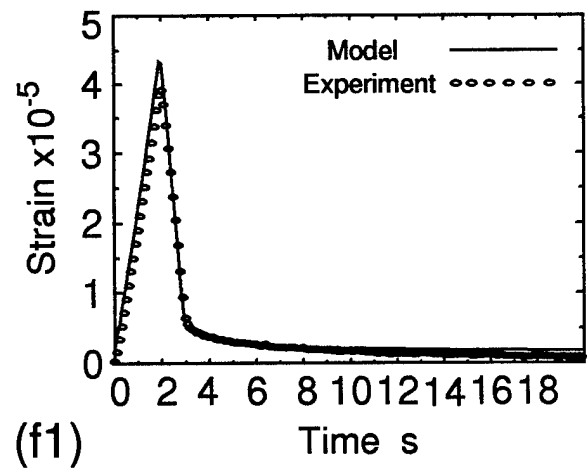
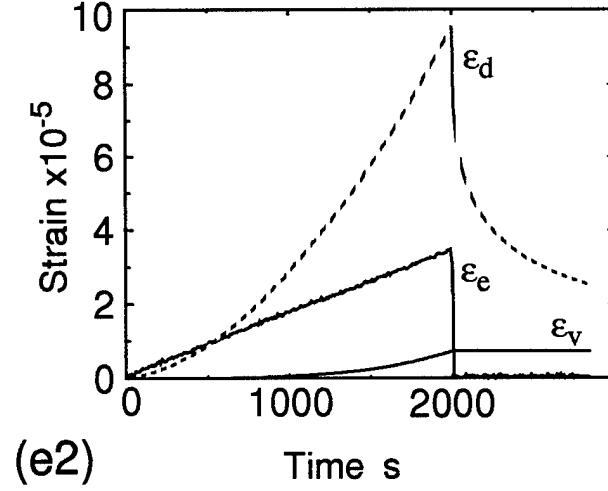
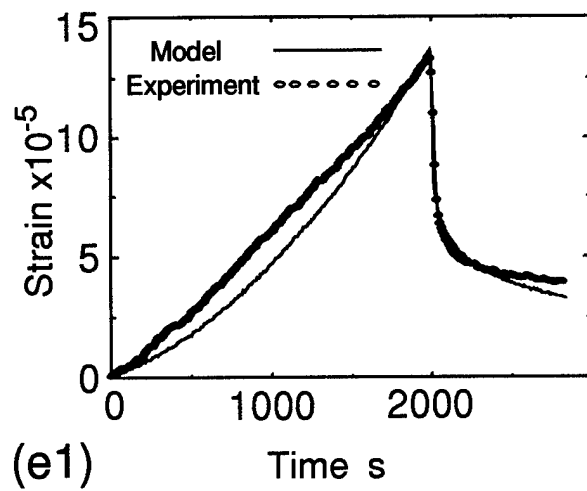
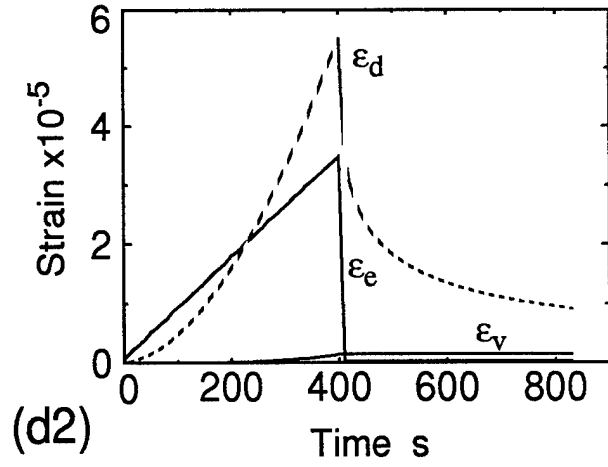
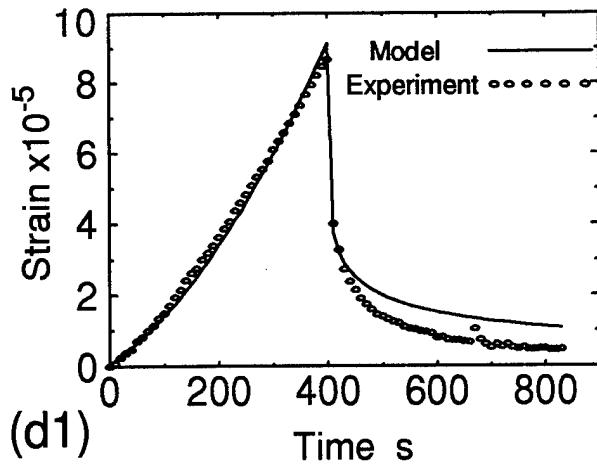


Figure 4.11: (d1) - (f1) Experimental and model strain response to monotonic stress ramps and (d2) - (f2) the individual strain components of each model.

4.7 Conclusion

The experiment described in the first section of this paper was designed based on nonlinear viscoelastic theory previously used in polymer research. Its purpose was to provide experimental data for investigating the constitutive characteristics of columnar S2 saline ice. The experiment was composed of two different uniaxial tensile stress loadings applied perpendicular to the columnar grain structure of a lab-grown, rectangular plate specimen. The first loading consisted of three creep-recovery loading sequences, applied at progressively higher stress levels. The second was a set of six monotonic ramps to the same preset peak stress, applied over a broad range of loading rates. All of the loading was accomplished with the modified RDS device. Using this apparatus, a constant uniaxial stress field was produced in the specimen with almost negligible rotation through the cross-section.

In the next section, a general equation for the strain response of saline ice to uniaxial, isothermal creep-recovery loading was derived. First, the total strain equation was expressed as the sum of three separate components: the elastic, the viscous and the delayed elastic strains. Then, using a Heaviside unit step function to represent the creep-recovery stress, and considering the special case when the stress functions $g_1 = a_\sigma = 1$, the equations for strain during both the creep and the recovery periods were determined. From this special case of nonlinear behavior (i.e. $g_1 = a_\sigma = 1$), it was shown that the recovery strain could be determined from the superposition of two creep strains. This characteristic, when generalized to an arbitrary number of cycles, was the basis of the numerical modeling effort.

After the equations were developed, the procedure for determining each of the model

parameters was given in detail. First, the elastic and delayed elastic strain components from the first creep segment at the two lowest stress levels were used to determine initial estimates of S_e , f_2 and $S_d(t)$. This was done iteratively by comparing the model results from various combinations of the three variables to the corresponding experimental data. Then, using the initial estimates, the remaining parameters were determined iteratively from the strain response due to all of the creep-recovery cycles. Through this investigation, the following values were determined for the general constitutive relation of saline ice subjected to uniaxial tensile stress, under isothermal conditions:

$$S_e = 13.5 \times 10^{-5} , S_1 = 0.08 \times 10^{-5} , S_2 = 8.25 \times 10^{-5}$$

$$p = 3 , q = 3/2 , n = 1/3 \quad (21)$$

Finally, the validity of this relation for modeling the response of saline ice to any arbitrary stress was verified by modeling the response of saline ice to monotonic ramp loadings. The model was applied to monotonic ramps with five different loading rates, ranging from 1 to 1000 N/s. Good correlation was observed between the model and the monotonic data at all loading rates, with the best occurring when the duration of the loading was similar to that of the creep-recovery cycles.

The results of this work are very encouraging for the use of a broad spectrum nonlinear viscoelastic constitutive equation in modeling the strain response of saline ice. However, more experiments must be performed before the definitive model parameters can be presented. Several improvements in the experimental procedure are immediately clear. First, the duration of the recovery period between creep loadings must be increased. In almost

every sequence, the ice was not allowed to fully recover the induced delayed elastic strain. Next, the creep loadings could be applied over longer durations and at higher stress levels. This would create a better database for evaluating the time and rate dependence of the model. And finally, in addition to the monotonic ramp loadings, it would be useful to apply sinusoidal cyclic and other in-situ based loadings to the specimen after completing the creep-recovery loadings. By doing so, the flexibility of this theory for modeling any arbitrary stress history will be most effectively examined.

5 REFERENCES

- Adamson, R.M., Dempsey, J.P., DeFranco, S.J., and Xie, Y., 1995. "Large-scale in-situ ice fracture experiments – Part 1: Experimental aspects." *Ice Mechanics 1995, ASME AMD* - Vol. 207, 107-128.
- Adamson, R. M., Dempsey, J. P. and Mulmule, S. V., 1995b. "Fracture analysis of semi-circular and semi-circular-bend geometries." *International Journal of Fracture*, (in press).
- Bentley, D. L., 1992. "Fracture of first-year sea ice: Preliminary results," *Proceedings of the 11th International OMAE Conference*, Vol. 4, 343-348.
- Chong, K. P., Kuruppu, M. D., 1984. "New specimen for fracture toughness determination of rock and other materials." *International Journal of Fracture*, 26, R59-R62.
- Cole, D. M., Gould, L. D., and Burch, W. B., 1985. "A system for mounting end caps on ice specimens." *Journal of Glaciology*, 31(109): 362-365.
- Cole, D. M. and Gould, L. D., 1989. "Uniaxial tension/compression tests on ice – preliminary results." *Proceedings of the 8th Offshore Mechanics and Arctic Engineering*, Vol. IV, pp. 37-41.
- Cole, D. M. and Gould, L. D., 1990. "Reversed direct-stress testing of ice: Equipment and example results." *Cold Regions Science and Technology*, 18(3): 295-302.
- Cole, D. M., 1990a. "Reversed direct-stress testing of ice: Initial experimental results and analysis." *Cold Regions Science and Technology*, 18(3): 303-321.
- Cole, D. M. and Durell, G. D., 1995a. "The cyclic loading of saline ice." *Philosophical*

- Magazine A*, 72(1): 209-229.
- Cole, D. M., 1995b. "A model for the anelastic straining of saline ice subjected to cyclic loading." *Philosophical Magazine A*, 72(1): 231-248.
- Cole, D. M. and Durell, G. D., 1995. "The effect of C-axis alignment on the constitutive behavior of sea ice at low strains." *ASME-AMD Vol. 207*, 189-199.
- Cole, D. M., Dempsey, J. P., Adamson, R. M., Shapiro, L. H., Petrenko, V. F. and Gluschenkov, O. V., 1995. "In-situ and laboratory measurements of the physical and mechanical properties of first-year sea ice." *ASME-AMD Vol. 207*, 161-178.
- Cox, G. F. N. and Weeks, W. F., 1983. "Equations for determining the gas and brine volumes in sea-ice samples." *Journal of Glaciology*, 29, 306-316.
- Currier, J. H. and Schulson, E. M., 1982. "The tensile strength of ice as a function of grain size." *Acta Metallurgica*, 30(8): 1511-1514.
- DeFranco, S. J. and Dempsey, J. P., 1992. "Nonlinear fracture analysis of saline ice: Size, rate, temperature effects." *IAHR 11th International Symposium of Ice*, Vol. 3, 1420-1436.
- DeFranco, S. J. and Dempsey, J. P., 1994. "Crack propagation and fracture resistance in saline ice." *Journal of Glaciology*, Vol. 40, 451-462.
- LeClair, E. S., Davey, C. and Dempsey, J. P., 1996. "A modified reversed direct-stress device." *Cold Regions Science and Technology*, (submitted).
- Lazo, J., 1994. "Fracture of saline ice: Thickness, orientation and reversed-direct tension testing." MS Thesis, Clarkson University, Potsdam NY, October.
- Langway, C. C., 1958. "Ice fabrics and the universal stage." CRREL Technical Report No.

- Lee, R. W., 1986. "A procedure for testing cored ice under uniaxial tension." *Journal of Glaciology*, 32 (112): 540-541.
- Mellor, M., Cox, G. F. N. and Bosworth, H., 1984. "Mechanical properties of multi-year sea ice; testing techniques." CRREL Technical Report, 84-8.
- Mulmule, S. V., Dempsey, J. P. and Adamson, R. M., 1995. "Large-scale in-situ ice fracture experiments – Part 2: Modeling aspects." *ASME AMD* Vol. 207, 129-146.
- Parsons, B. L., Snellen, J. B. and Hill, B., 1986. "Physical modeling and the fracture toughness of sea ice." *Proceedings of the 5th OMAE Conference*, Vol. IV, 358-364.
- Richter-Menge, J. A. and Jones, K. F., 1993. "The tensile strength of first-year sea ice." *Journal of Glaciology*, 39 (133): 609-618.
- Richter-Menge, J. A., Claffey, K. J. and Walsh, M. R., 1993. "End-capping procedure for cored ice samples used in tension tests." *Journal of Glaciology*, 39 (133): 698-700.
- Schapery, R. A., 1969. "On the characterization of nonlinear viscoelastic materials." *Polymer Engineering and Science*, 9(4): 295-310.
- Schapery, R. A., 1996. "Thermomechanical constitutive equations for polycrystalline ice." *Proceedings of the 13th IAHR Symposium on Ice*, Beijing, China.
- Schwarz, J., Frederking, R., Gavrillo, V., Petrov, I. G., Hirayama, K. I., Mellor, M., Tryde, P. and Vaudrey, K. D., 1981. "Standardized testing methods for measuring mechanical properties of ice." *Cold Regions Science and Technology*, 4: 245-253.
- Shapiro, L. H., Metzner, R. C. and Johnson, J. B., 1981. "Fracture toughness of sea ice."

Report submitted to the Shell Development Company.

- Shapiro, L. H. and Weeks, W. F., 1995. "Controls on the flexural strength of small plates and beams of first-year sea ice." *ASME-AMD* Vol. 207, 179-188.
- Shen, W. and Lin, S. Z., 1986. "Fracture toughness of Bohai Bay sea ice." *Proceedings of the 5th International OMAE*, Vol. IV, 354-357.
- Sinha, N. K., 1989. "Closed-loop controlled tensile strength testing method for multi-year sea ice." *Proceedings of the 8th OMAE*, Vol. IV, 1-6.
- Timco, G. W. and Frederking, R. M. W., 1982. "Flexural strength and fracture toughness of sea ice." *Cold Regions Science and Technology*, 8, 35-41.
- Urabe, N. and Yoshitake, A., 1980. "Fracture toughness of sea ice." *Cold Regions Science and Technology*, 3, 29-37.
- Urabe, N. and Yoshitake, A., 1981a. "Strain rate dependent fracture toughness (K_{IC}) of pure ice and sea ice." *Proceedings of the 6th IAHR Ice Symposium*, Vol. II, 410-420.
- Urabe, N. and Yoshitake, A., 1981b. "Fracture toughness of sea ice - In-situ measurement and its application." *Proceedings of the 6th IAHR Ice Symposium*, Vol. I, 356-365.
- Urabe, N. and Inoue, M., 1986. "Mechanical properties of Antarctic sea ice." *Proceedings of the 5th International OMAE*, Vol. IV, 303-309.
- Tuhkuri, J., 1987. "The applicability of LEFM and the fracture toughness to sea ice." *Proceedings of the 8th Port and Ocean Engineering Under Arctic Conditions*, Vol. I, 21-32.
- Weeks, W. F. and Gow, A. J., 1979. "Crystal alignments in the fast ice of arctic Alaska."

CRREL Report 79-22.

Williams, F. M., Kirby, C. and Slade, T., 1993. "Strength and fracture toughness of first year arctic sea ice." Institute for Marine Dynamics, NRC Canada, Report No. Tr-1993-12.

Vaudrey, K. D., 1977. "Ice engineering-study of related properties of floating sea ice sheets and summary of elastic and viscoelastic analyses." Technical Report 860, Civil Engineering Laboratory, Naval Construction Battalion Center, Port Hueneme, California.

6 PUBLICATIONS

6.1 JOURNAL PUBLICATIONS

E. S. LeClair, C. Davey and J. P. Dempsey, "A modified reversed direct-stress device," *Cold Regions Science and Technology* (accepted for publication).

E. S. LeClair, R. M. Adamson and J. P. Dempsey, "Core-based SCB fracture (Phase VI) of aligned first year sea ice," *ASCE Journal of Cold Regions Engineering* **11** (1997) (to appear).

E. S. LeClair, R. A. Schapery and J. P. Dempsey, "A broad-spectrum constitutive model for saline ice," *International Journal of Fracture* (in preparation).

6.2 CONFERENCE PUBLICATIONS

E. S. LeClair, R. A. Schapery and J. P. Dempsey, "Tensile creep of saline ice," ' *Symposium on Inelasticity and Damage in Solids Subject to Microstructural Change*, St. John's, NF, September 25-27 (1996) (in press).